Check for updates

*Small*

NANO · MICRO small
www.small-journal.com

RESEARCH ARTICLE OPEN ACCESS

# Three-Dimensional Optical and Computational Reconstruction of Colloidal Electrokinetic Flows via Multiplane Imaging and Multiscale Modeling

Flip de Jong[1] | Pablo Diez-Silva[2] | Jui-Kai Chen[1] | Raúl P. Peláez[2] | Sudipta Seth[1] | Bing-Yang Shih[3] | Senne Fransen[3] | Radin Tahvildari[3] | Kruti Trivedi[3] | Rémi Pelletier[4] | Harishankar Balakrishnan[5] | Carmen Hervés-Carrete[6,7,8] | Carlos Renero-Lecuna[6,7,8] | Willem Van Roy[3] | Maarten Rosmeulen[3,9] | Santi Nonell[5] | Susana Rocha[1] | Andrey Klymchenko[4] | Luis M. Liz-Marzán[6,7,8] | Roger Bresolí-Obach[5] | Manuel I. Marqués[10] | Johan Hofkens[1] | Rafael Delgado Buscalioni[2] | Boris Louis[1]

[1]Department of Chemistry, Molecular Imaging and Photonics, KU Leuven, Leuven, Belgium | [2]Department of Theoretical Condensed Matter Physics, Universidad Autónoma de Madrid, and Condensed Matter Physics Institute (IFIMAC), Madrid, Spain | [3]imec, Leuven, Belgium | [4]Laboratoire de Bioimagerie et Pathologies, UMR 7021 CRS, Université de Strasbourg, Illkirch, France | [5]Department of Analytical and Applied Chemistry, AppLightChem, Institut Quimic de Sarria, Universitat Ramon Lull, Barcelona, Catalunya, Spain | [6]CINBIO, University de Vigo, Vigo, Spain | [7]CIC biomaGUNE, Basque Research and Technology Alliance (BRTA), Donostia-San Sebastián, Spain | [8]Ikerbasque, Bilbao, Spain | [9]KU Leuven, Department of Electrical Engineering, Leuven, Belgium | [10]Departamento de Física de Materiales & Condensed Matter Physics Center (IFIMAC) & Nicolás Cabrera Institute, Universidad Autónoma de Madrid, Madrid, Spain

**Correspondence:** Johan Hofkens (johan.hofkens@kuleuven.be) | Rafael Delgado Buscalioni (rafael.delgado@uam.es) | Boris Louis (boris.louis@kuleuven.be)

**Received:** 22 March 2026 | **Revised:** 24 July 2026 | **Accepted:** 29 July 2026

**Keywords:** 3d microscopy | colloid | dielectrophoresis | electric field | electrokinetic phenomena | microfluidics | multiscale modeling | nanoparticle | nanotechnology | single-particle tracking

## ABSTRACT

Sorting, filtering, and controlling colloidal particles is crucial in many fields, ranging from chemistry to biology and physics. Dielectrophoresis (DEP) enables selective manipulation of colloids by non-uniform AC electric fields, yet the associated three-dimensional nanoparticle dynamics and electrokinetic flows remain difficult to access experimentally. Here, we combine real-time multiplane widefield microscopy (> 100 fps), 3D single-particle tracking, and multiscale modeling to reconstruct the motion of 200 nm fluorescent polystyrene nanoparticles around a quadrupolar electrode under positive and negative DEP. This optical–computational approach provides volumetric trajectories and flow maps, revealing particle trapping, depletion, and three-dimensional vortical motion. A model including DEP and AC electro-osmotic flow quantitatively reproduces the positive DEP dynamics, demonstrating direct agreement between experiment and theory. Under negative DEP, the model captures particle depletion near the electrodes but not all observed flow structures, pointing to additional electrokinetic or electrothermal contributions. This framework provides a route to validate and refine AC electrokinetic models for complex colloidal and microfluidic systems.

**Abbreviations:** DEP, dielectrophoresis; pDEP, positive dielectrophoresis; nDEP, negative dielectrophoresis; EK, electrokinetics; AC, alternating current; fps, frames per second; PS, polystyrene; MPM, multiplane widefield microscopy; NP, nanoparticle; SPT, single particle tracking; PSF, point spread function; PCB, printed circuit board; CMOS, complementary metal-oxide semiconductor; sCMOS, scientific CMOS; N.A., numerical aperture; EDL, electrical double layer; CM, Clausius-Mossotti; BC, boundary condition; GMRES, Generalized Minimal Residual (iterative solver); IBM, Immersed Boundary Method; MES, 2-(N-morpholino)ethanesulfonic acid; PMMA-MA, Polymethyl methacrylate-comethacrylic acid; ALD, Atomic Layer Deposition; PVD, Physical Vapor Deposition.

Flip de Jong and Pablo Diez-Silva contributed equally to this work.

This is an open access article under the terms of the Creative Commons Attribution-NonCommercial License, which permits use, distribution and reproduction in any medium, provided the original work is properly cited and is not used for commercial purposes.
© 2026 The Author(s). *Small* published by Wiley-VCH GmbH

## 1 | Introduction

Selective manipulation of particles is essential in fields such as chemical and biological analysis, food processing, environmental assessment, diagnostics, and cell assays [1, 2]. For example, in biomedicine sorting is used to distinguish healthy from diseased cells [3], while in materials science precise particle arrangement determines collective properties, as is the case for photonic crystals or metamaterials [4]. This manipulation depends on the particles' physical properties (e.g., size, shape, charge), chemical properties (e.g., material behavior, polarity, solvent/suspension medium), and external force fields (e.g., optical, magnetic, electric) [5, 6]. Among the techniques used to manipulate small particles, dielectrophoresis (DEP) stands out for its rapid and highly selective abilities [7–10].

Electrophoresis is widely employed to separate biomolecules based on their size and charge under a uniform electric field. In contrast, in the less explored dielectrophoresis (DEP) polarizable particles interact with a non-uniform field. DEP offers a significant advantage, as it can selectively manipulate and separate not only charged species, but also neutral particles by exploiting differences in polarizability. This capability makes DEP a more versatile and powerful tool for advanced applications in materials science. One example is the recent progress toward a colloidal memory [11, 12]. In DEP, particles become polarized under an external field, with an induced dipole moment proportional to the field itself. In turn the non-uniform electric field exerts a force on the induced dipole. Consequently, the DEP force scales quadratically with the electric field strength. This leads to a net force with non-zero time average, even under alternating (AC) fields, which can attract or repel particles toward regions of high electric field density. The direction of the DEP force is determined by the net polarizability, which for relatively large particles (> 100 nm) is described well by the Clausius–Mossotti factor ($f_{\mathrm{CM}}$, see Equation (5)) [13]. This factor depends on the dielectric contrast, i.e., the difference between the complex electric permittivities of the particle ($\tilde{\varepsilon}_p$) and the medium ($\tilde{\varepsilon}_m$). If the polarizability of the particle is positive, the particle experiences what is called positive DEP (pDEP) and moves toward the region of higher electric field density (this mode is commonly used to trap particles). Conversely, if the particle's polarizability is negative, it experiences negative DEP (nDEP) and is repelled toward regions of lower electric field density [7]. Importantly, $f_{\mathrm{CM}}$ is frequency-dependent. Moreover, the use of electrolyte solutions induces AC electrokinetic flows, which further complicate the dynamics of nanoparticles (NPs).

Several studies have used DEP to investigate biological elements like DNA [14], cells [15], tumor cells [16, 17], bacteria [18], viruses [19, 20], and nanostructures like isotropic NPs [7, 19, 21], nanotubes [22], and nanowires [23]. Despite these advances, accurately characterizing and simulating the electrokinetic behavior of small particles under alternating electric fields remains challenging due to the multiscale nature of the problem. Current models that incorporate both DEP forces and electrokinetic flow are typically limited to micron-sized particles [24]. While techniques such as impedance [20, 25–27], light scattering/extinction [28–30], and fluorescence correlation spectroscopy [31] have been used to measure the accumulation or depletion of colloids under electric fields, microscopy offers a more detailed picture, resolving the spatial position of particles and their motion. Morgan and coworkers were among the first to use (2D) fluorescence microscopy to visualize dielectrophoretic trapping of submicrometer particles [32–35] and gave an instructive overview of the observed AC electrokinetics [36] [37]. Additional information can be extracted by recording the position of single particles over the frames of a video, focusing for example on trapping statistics at the electrodes [35, 38] or on single particle trajectories for velocity analysis [39, 40]. In contrast to these 2D fluorescence movies, real-time 3D measurements can yield the full particle dynamics and if the concentration of imaged particles is sufficiently high, they allow visualization of the particle response to the electric field for the full imaged volume. Such volumetric measurements can also support the design, validation, and optimization of emerging three-dimensional DEP electrode architectures, such as those recently proposed in [41]. A first example is provided by Stanke et al., who used a mirror to obtain simultaneous access to a top and a side view of the sample, and used manual tracking of a few particles to obtain their velocities [42]. Another approach is to use only one plane that is selected to be close to a wall (for example the electrodes) and then use the degree to which the particle is out of focus to determine their distance from the selected plane, converting 2D light microscopy videos to 3D tracking information [43, 44]. This is related to other point spread function (PSF) engineering work [45, 46], but suffers from errors induced by overlapping PSF at higher concentration. Likewise, attempts using interdigitated transducer electrodes [47], confocal microscopy [48] or digital holography [49] have not yet delivered the consistent, high spatial resolution tracking required for the reconstruction of detailed motion and speed maps.

Here, we use a custom-designed MultiPlane widefield Microscope (MPM) [50–52] that allows imaging of a large volume in real-time without strict constraints on particle concentration, enabling tracking of a large number of particles and statistical analysis of the localization and velocities of the tracked particles. MPM simultaneously records eight images (planes) at different z-depths covering a volume of $40 \times 60 \times 4\,\mu\mathrm{m}^3$, enabling real-time, true 3D imaging. We use this technique to track 200 nm carboxylate-modified polystyrene (PS) NPs under dielectrophoresis conditions in 3D and map the AC electric field-induced flows around a quadrupolar electrode, a geometry chosen for its widespread use in literature [36]. This is the first application of MPM in the field of colloidal electrokinetics. The particle type investigated in this work was selected based on a preliminary experimental screening campaign performed at imec. These preliminary experiments showed that the particle-condition combination (200 nm carboxylate-modified PS NP in 0.1 mM KCl at pH 6.0) is characterized by a pronounced DEP response and a well-defined cross-over frequency in an experimentally accessible frequency window of 2.3–2.4 MHz. To understand the physical effects dictating NP behavior a dedicated modeling approach was developed to qualitatively and quantitatively explain the experimental results. Briefly, we computed the electric field and the dielectrophoretic force using finite differences, and we solved the electrokinetic flows with a novel formalism based on particle discretization of the fluid and Green propagator. We show experimental and modeling results for two conditions, corresponding to a pDEP and nDEP condition. The visualized particles are either (i) trapped in the space between the electrodes, (ii) moving on top of the electrodes or (iii) moving toward



16136829, 2026, 58, Downloaded from https://onlinelibrary.wiley.com/doi/10.1002/smll.75129, Wiley Online Library on [10/11/2026]. See the Terms and Conditions (https://onlinelibrary.wiley.com/terms-and-conditions) on Wiley Online Library for rules of use; OA articles are governed by the applicable Creative Commons License

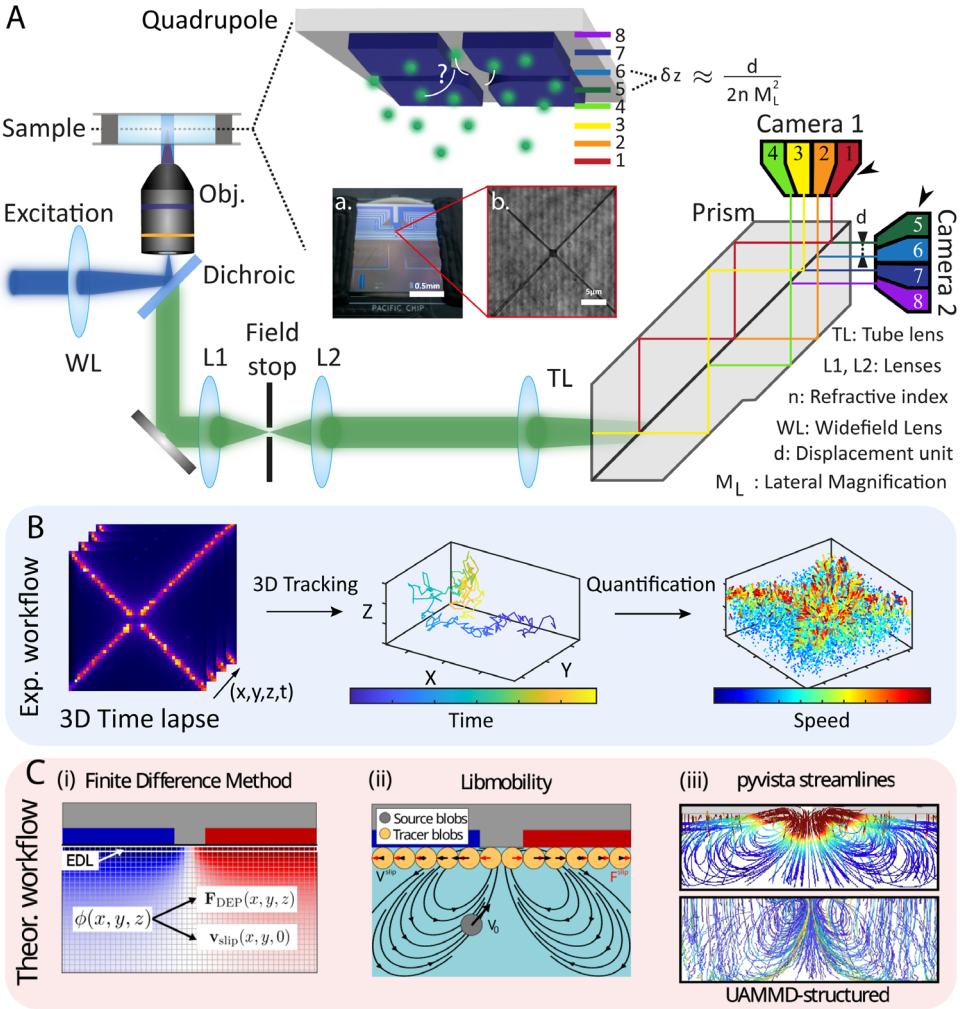



**Figure 1** | 3D imaging experimental setup with experimental and theoretical workflows: (A) a 488 nm laser is focused on the back aperture of the objective to generate widefield illumination. The light emitted from the sample is collected via an 8f system, where a prism beamsplitter splits the image in 8, each of the split paths having a different optical path length. This leads to eight images focused at different depth inside the sample, resulting in a true volumetric image. The top focal plane is aligned with the electrode surface. The images are collected 4 by 4 by two synchronized sCMOS. (a) Photograph of the microfluidic device containing the quadrupole electrode. (b) Scattering image of the quadrupole electrode under the microscope. (B) Experimental workflow: A 3D time lapse of the imaged volume is acquired under application of an alternating electric field. Individual particles are tracked in 3D, and their speed is calculated and mapped out in all dimensions. (C) Theoretical workflow: (i) The potential $\phi(\mathbf{r})$ is calculated via a finite difference method in a regular mesh. This leads to the electric field and to the dielectrophoretic force $F_{\mathrm{DEP}}$. Also, $\phi$ determines the ion slip velocity at the EDL layers $v_{\mathrm{slip}}$, which is (ii) propagated to the bulk to calculate EK flow in all the system using `libMobility` [53]. (iii) The deterministic NP velocity field is illustrated using `PyVista` streamlines [54] and the NP dynamics are solved with `UAMMD-structured` Brownian solver [55].

or away from the device. This comprehensive picture provides an unprecedented level of detail in the field of electrokinetics and is applicable to any electrode geometry as well as other colloidal systems. The combined MPM/modeling methodology can contribute to a deeper understanding of electrokinetic and other effects at the nanoscale, which can lead to advances in particle manipulation and sorting across disciplines including physics, chemistry, microelectronics, biology and medicine.

## 2 | Multiplane Microscopy and Dielectrophoresis Setups

To experimentally investigate NP motion under DEP, we employed a simple quadrupolar electrode (total area ($100 \times 100$) $\mu$m$^2$, with a separation between the electrodes of 600 nm and a depth of the trench (inter-electrode corridor) of 50 nm) connected to a PCB board and driven by a Keysight waveform generator (EDU33212A) which was controlled by a homemade LabVIEW program. The quadrupole device is schematically depicted in Figure 1 along with a picture of the chip (1A) and a backscattering image of the quadrupole (1B).

For three-dimensional NP tracking, we used our custom-built multiplane microscope [51], as shown in Figure 1A. Briefly, a prism beam splitter divides the detected emission into eight separate images, four collected on each of the two synchronized sCMOS cameras. The prism's geometry creates different optical path lengths between the tube lens and the cameras, conjugating eight distinct z-planes within the sample to 8 different images



16136829, 2026, 58, Downloaded from https://onlinelibrary.wiley.com/doi/10.1002/smll.75129, Wiley Online Library on [10/11/2026]. See the Terms and Conditions (https://onlinelibrary.wiley.com/terms-and-conditions) on Wiley Online Library for rules of use; OA articles are governed by the applicable Creative Commons License

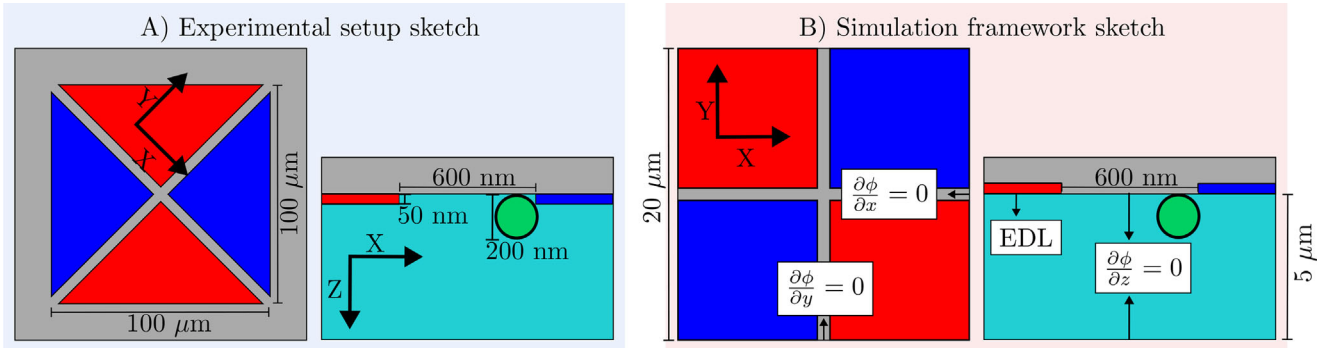



**Figure 2** | Quadrupole schematic. (A) Experiment. Top and side view of a schematic representation of the quadrupole device. The corridor is not to scale in the top view. The base of the electrodes is 100 $\mu$m long, the separation between electrodes is 600 nm. (B) Simulation framework. Top and side view of a schematic representation of the quadrupole device used in the simulations with the boundary imposed to the electric potential indicated. The EDL boundary condition refers to the Electric Double Layer boundary condition explained in the main text: $\sigma_m\,\partial\phi/\partial z = (\phi - V_0)/Z_{DL}$. The simulation framework only models the center of the quadrupole, with a domain size of $20 \times 20 \times 5$ $\mu$m. Note that in the experimental device the height of the electrode above the dielectric is 50 nm (A). Since this height is smaller than the NP radius, the model electrode is simplified to be fully coplanar with the dielectric substrate. This approximation has a limited effect on the description of the behavior in the bulk.

on the detector. In this work we use an inverted microscope, where the focal plane is positioned to have the top plane near the electrode interface (Figure 1A). The electrodes are therefore facing down toward the solution, in contrast to typical images in literature. The multiplane microscope enables imaging of a volume of $50 \times 50 \times 4\,\mu m^3$ at a high frame rate (125 fps). An example raw image of the multiplane data is shown in Figure S3. Calibration was performed as previously described [51] and determined an inter-plane distance of approximately 580 nm (see Figure S2), with tracking precision 10 nm (x-y) and 20 nm (z), and accuracy of 20 nm (x–y) and 40 nm (z) [51].

### 2.1 | 3D Visualization and Modeling of 200 nm PS Particles Under Positive and Negative Dielectrophoresis

To visualize the dynamics of 200 nm PS particles under DEP, we first established the voltage and frequency regimes for pDEP and nDEP. We then optimized the voltage to ensure that particles did not move too fast nor too slow, allowing accurate visualization at 125 fps. Two conditions were selected: 100 kHz at an amplitude of 0.5 V to show pDEP, and 5 MHz at 1 V where the PS particles experience nDEP. The experimental workflow is schematically described in Figure 1B. Briefly, a 10 s (1250 frames at 125 fps) 3D time lapse was acquired during which an alternating electric field was applied at the desired voltage and frequency. For each movie, we then tracked the particles in 3D, using our custom software (freely available at https://github.com/BorisLouis/3D-image-processing) [51]. Finally, we determined the speed and combined the data of 10 different movies to increase the statistics and allow mapping of the speed of the particles in the 3D space.

Using the fast 3D imaging afforded by MPM, we could directly observe how particles move under different conditions around a quadrupolar electrode. This experimental information provides a quantitative measure on the DEP force field and accompanying electrokinetic flows, and establishes a solid base to validate the theoretical and modeling approach. One of the advantages of particle tracking is that it allows one to measure the "instantaneous" particle velocity. The particle position is denoted as $\mathbf{R}(t)$ and $\Delta\mathbf{R}(t) = \mathbf{R}(t + \Delta t_{\text{sample}}/2) - \mathbf{R}(t - \Delta t_{\text{sample}}/2)$ and so the particle velocity is $\mathbf{v}_p = \Delta\mathbf{R}/\Delta t_{\text{sample}}$ with $\Delta t_{\text{sample}} = (1/125)$ s the sampling frequency of experimental frame. This experimental quantity can be directly compared with simulations and theory.

## 3 | Theory and Modeling

Our modeling approach reproduces the central part (area $20 \times 20\,\mu m^2$) of the experimental quadrupole, described as a microfluidic chip of four metallic plate electrodes on a dielectric (silica) substrate and inside an electrolyte fluid (water). Figure 2 compares the electrodes used by the experimental and modeling setups. The four electrodes are connected to an AC voltage of amplitude $V_0$ and frequency $\omega$ and adjacent plates present a phase difference in voltage of $\pi$. Note that the AC field is monochromatic, so any field can be described using a phasor. In particular, the time dependent potential is expressed as $\Re\{\phi(\mathbf{r})\exp[i\omega t]\}$. Our target is to solve the dynamics of spherical polystyrene (PS) dielectric NPs of radius $a = 100$ nm (we refer to them as 200 nm NPs, after their diameter). Figure 1C illustrates the modeling protocol. First (Figure 1C(i)) we evaluate the complex potential field $\phi(\mathbf{r})$ using the finite difference method on a regular mesh. The potential $\phi$ directly provides the two main driving effects: the DEP force arising from the inhomogeneous electric field and the electrokinetic (EK) flow due to AC electro-osmosis close to the electrodes [56]. While the DEP force $\mathbf{F}_{\text{DEP}}(\mathbf{R})$ is evaluated at the NP locations $\mathbf{R} \equiv \{\mathbf{R}_1, \ldots, \mathbf{R}_N\}$, the EK flow needs to be determined from the effective fluid slip velocity $v_{\text{slip}}(\mathbf{r})$ field created adjacent to the electrodes by the ion oscillatory flows inside the charged electric double layers (EDL). Note that the EK flow has a fast oscillatory (jiggling) component (frequency $\omega \in$ [kHz – MHz]) and a relevant stationary resultant $\mathbf{v}_0(\mathbf{r})$ which drives the NPs by advection. To calculate $\mathbf{v}_0(\mathbf{r})$ we follow a multiscale approach, imposing $v_{\text{slip}}(\mathbf{r})$ as a boundary condition. We use a novel procedure which involves an array of "source blobs" (orange circles in Figure 1C(ii)) where we impose "slip" electric forces $\mathbf{F}_{\text{slip}}$ which self-consistently generate the required slip field $v_{\text{slip}}[\phi]$ close to the $z = 0$ boundary, corresponding to



16136829, 2026, 58, Downloaded from https://onlinelibrary.wiley.com/doi/10.1002/smll.75129, Wiley Online Library on [10/11/2026]. See the Terms and Conditions (https://onlinelibrary.wiley.com/terms-and-conditions) on Wiley Online Library for rules of use; OA articles are governed by the applicable Creative Commons License

the device surface. The momentum resulting from $\mathbf{F}_{\text{slip}}$ is then transferred to the bulk-fluid (using appropriate fluid-dynamic Green's functions) to create the electrokinetic (EK) flow $\mathbf{v}_0(\mathbf{r})$ illustrated in Figure 1C(iii). These two effects (DEP forces and EK flow) provide the deterministic component for the particles' motion. However, it is essential to include the particles' random (Brownian) displacements to properly describe their dynamics. As illustrated in Figure 1C(iii, bottom), Brownian displacements alter the NP trajectories, and their relevance strongly depends on the determinist flow intensity.

The aqueous solution has a viscosity $\eta \approx 0.001$ Pa · s and density $\rho \approx 10^3$ kg/m$^3$. Due to the small size of the NPs, fluid inertia can be fully neglected. Moreover, the NP density ($\sim 1.05\rho$) is similar to that of the fluid and therefore NP inertia and buoyancy are negligible, as it corresponds to the Stokes regime. The time-evolution of the individual NP positions $\mathbf{R} \equiv \{\mathbf{R}_i\}$ can therefore be described by standard Brownian dynamics (BD) equations [57],

$$d\mathbf{R} = \mathbf{v}_0(\mathbf{R})dt + \mu[\mathbf{F}_{\text{DEP}} + \mathbf{F}_{\text{wall}}]dt + \delta\tilde{\mathbf{R}} \tag{1}$$

where the first term in the right-hand side corresponds to the EK flow advection $\mathbf{v}_0(\mathbf{R})$ interpolated at the particle location $\mathbf{R}$. Besides the DEP force $\mathbf{F}_{\text{DEP}}$, we add $\mathbf{F}_{\text{wall}}$ corresponding to short-ranged excluded volume interactions with the system's boundaries. The experimental NP concentration is very dilute (around $5 \times 10^{-3}$ $\mu$m$^{-3}$, or volume fraction $\sim 10^{-5}$) which allows us to neglect all type of NP-NP interactions (i.e., hydrodynamic couplings, dipole-dipole and excluded volume interactions). The self-mobility of each NP is $\mu = (6\pi\eta a)^{-1}$ and the NP diffusion coefficient is $D = k_B T\mu$. Finally, in Equation (1), the vector of random NP displacements is noted as $\delta\tilde{\mathbf{R}}$. It satisfies the fluctuation dissipation relation $\langle\delta\tilde{\mathbf{R}}\delta\tilde{\mathbf{R}}^T\rangle = 2Ddt$ by applying the standard ansatz $\delta\tilde{\mathbf{R}} = \sqrt{2D}\,\delta\mathbf{W}$ built from independent Wiener increments $\langle\delta\mathbf{W}\delta\mathbf{W}^T\rangle = \mathbf{I}\,dt$ (with $\mathbf{I}$ the identity matrix).

### 3.1 | AC Potential

As stated, the evaluation of DEP forces and EK flow requires solving the AC potential $\phi(\mathbf{r})$. To this end, we note that the free charge density only differs from zero inside the EDLs adjacent to the electrode surface. In the bulk, the fluid is electro-neutral, so $\phi$ is determined by the Laplace equation $\nabla^2\phi = 0$. The boundary conditions (BCs) for $\phi(\mathbf{r})$ are illustrated in Figure 2B. At the bottom of the trench between the electrodes (grey domains in Figure 2B) water permittivity is much larger than that of the bottom dielectric walls so the electric field in the normal $\mathbf{n}$ direction is approximately zero $\nabla\phi \cdot \mathbf{n} = 0$ (i.e. no current flows through the dielectric). To derive the BC at the surface of the electrodes we use an equivalent RC circuit. For large enough ionic strength and for the particle sizes considered here, the EDL width (the Debye length $\lambda_D$) is small compared to any other system's scale $\lambda_D/L \ll 1$. Following Ramos et al. [36, 56] we thus treat the charged Debye layer as a capacitor providing a consistent effective BC applied at the thin layer,

$$\sigma_m\,\nabla\phi \cdot \mathbf{n} = \frac{1}{Z_{DL}}(\phi - V_0) \tag{2}$$

The gradient in Equation (2) is taken along the normal-to-wall coordinate $\mathbf{n}$. The medium's conductivity is $\sigma_m$ and $Z_{DL}$ is the impedance associated to the EDL which we assume to be a perfect capacitor, i.e., $Z_{DL}^{-1} = i\,\omega C$ with capacitance $C = \varepsilon/\lambda_D$[1]. The Debye length $\lambda_D$ for our 1:1 electrolyte is,

$$\lambda_D = \left(\frac{\varepsilon k_B T}{n_0 q^2}\right)^{1/2} \tag{3}$$

with $q = e$ the electron charge, $T \simeq 300$ K the temperature, $\varepsilon = \varepsilon_r\varepsilon_0$ the absolute dielectric permittivity of the medium and $n_0$ the ion concentration. Introducing the dimensionless frequency $\Omega = \omega\varepsilon L/(\sigma\lambda_D)$, the BC of Equation (2) becomes $\nabla\phi \cdot \mathbf{n} = i\Omega(\phi - V_0)$. Thus, it is evident that if $\Omega \ll 1$ the electrolyte will fully screen the electric field within the EDL, yielding a Neumann BC $\nabla\phi \cdot \mathbf{n} = 0$. In the other limit, $\Omega \gg 1$, the ions do not have time to adapt to the fast electric field and the effective double layer length is shortened, leading to $\phi = V_0$. We use a regular mesh to solve the electrostatic potential in the relevant central portion of the experimental 100 $\mu$m-side quadrupole. The box sides ($L_x = L_y = 20\,\mu$m and $L_z = 5\,\mu$m) are far away enough to consider Neumann BCs $\nabla\phi \cdot \mathbf{n} = 0$ at $x = \pm L_x/2$ and $y = \pm L_y/2$ and $z = L_z$ (see Figure 2).

### 3.2 | Dielectrophoretic Forces $\mathbf{F}_{\text{DEP}}$

The resulting electric field $\mathbf{E} = -\nabla\phi$ leads to the DEP force on the NPs. A particle with polarizability $\alpha$ under an external field $\mathbf{E}$ presents an induced dipolar moment $\alpha\mathbf{E}$ and an instantaneous electrostatic force $\alpha\mathbf{E} \cdot \nabla\mathbf{E}$. In an inhomogeneous AC field this yields a non-vanishing temporal average, which in terms of phasor fields is given by,

$$\mathbf{F}_{\text{DEP}} = \frac{1}{2}\Re\{\alpha\}\nabla|\mathbf{E}|^2 \tag{4}$$

which is the DEP force written in conservative form (i.e., as the gradient of an effective potential energy $U_{\text{DEP}} = -\frac{1}{2}\Re\{\alpha\}|\mathbf{E}|^2$). Notably, the fate of the NP depends on the real part of its polarizability: if $\Re\{\alpha\} > 0$ the DEP force points toward the maxima of the electric field intensity $E^2$, described as pDEP. Conversely, if $\Re\{\alpha\} < 0$, the DEP force drives the particle toward low field regions, which is called nDEP. For the moderately large size of our NPs ($\sim 200$ nm in diameter) it is possible to use the Clausius-Mossotti relation to calculate $\alpha(\omega)$ and include the contribution from the ion conductivity $\sigma$ according to the Maxwell-Wagner approximation, leading to $\alpha = 4\pi a^3\varepsilon_m\varepsilon_0 f_{\text{CM}}$ where the Clausius–Mossotti (CM) factor $f_{\text{CM}}$ is,

$$f_{\text{CM}} = \frac{\tilde{\varepsilon}_p - \tilde{\varepsilon}_m}{\tilde{\varepsilon}_p + 2\tilde{\varepsilon}_m} \tag{5}$$

with subscripts $p$ and $m$ referring to the particle and the medium, respectively, and where the complex permittivity is defined as $\tilde{\varepsilon} = \varepsilon - i\sigma/\omega$. Note that $f_{\text{CM}}$ determines the sign of the DEP force, resulting in either pDEP or nDEP.



16136829, 2026, 58, Downloaded from https://onlinelibrary.wiley.com/doi/10.1002/smll.75129, Wiley Online Library on [10/11/2026]. See the Terms and Conditions (https://onlinelibrary.wiley.com/terms-and-conditions) on Wiley Online Library for rules of use; OA articles are governed by the applicable Creative Commons License

### 3.3 | Electrokinetic Flow, $\mathbf{v_0}(\mathbf{r})$

AC electrokinetic flow is nicely explained by Ramos et al. [58]. A net slip flow is created inside the Debye layer due to the non-vanishing electric field component in the horizontal directions $\mathbf{s} = (x, y)$, parallel to the electrode plane. Within the charged layers adjacent to the electrodes $\nabla\phi \cdot \hat{\mathbf{s}} \neq 0$ (where $\hat{\mathbf{s}}$ is the unitary vector in the plane), and this is pushing the ions and creating a net (averaged) tangential flow with a "slip" velocity,

$$\mathbf{v}_{\text{slip}} = -\Lambda \frac{\varepsilon}{4\eta} \hat{\mathbf{s}} \cdot \nabla(|\phi - V_0|^2)\, \hat{\mathbf{s}} \tag{6}$$

Where $\Lambda$ is the ratio between the diffuse layer potential drop and the total double layer potential drop [58]. This parameter is commonly used to fit theory to experiment. In this work, a $\Lambda$ value between 0.3 and 0.8 gives a good agreement with experiments. To allow a direct comparison between different conditions, we fixed $\Lambda = 0.5$ for all calculations.

This tangential flow propagates by continuity of the liquid to the bulk, creating an electrokinetic flow $\mathbf{v}_0(\mathbf{r})$ composed of pairs of counter-rotating vortices, which is discussed in Results and Discussion. The standard way to solve this flow consists of imposing the slip BC in Equation (6) at the electrodes' surface and solve the Navier–Stokes equations in a finite box, meshed via finite differences to obtain $\mathbf{v}_0(\mathbf{r})$ everywhere. However, this standard route introduces some technical problems: the system is unbounded in the plane directions (x,y) and a finite box will always introduce hydrodynamic finite size effects. Moreover, new electrode designs require re-meshing and modifying the BCs. Also note that the slip BC in Equation (6) corresponds to a coarse-grained view of the flow within the Debye layers, whose real structure locally resembles a Blasius flow layer with no-slip at the electrode surface and a current above it. Here we use an alternative formalism based on particle discretization of the fluid and the Green propagator which fully circumvents these problems and permits a seamless connection with NP dynamics, as schematically represented in Figure 1C(ii). This new computational formalism uses the `libMobility` [53] library and has been validated against traveling wave electro-osmosis experiments [59]. The slip flow is introduced through a force density distribution $\mathbf{f}_{\text{slip}}(\mathbf{r})$, localized within the Debye layer ($\lambda_D \approx 40$ nm using Equation (3)), which propagates flow into the bulk via the Blake Green's tensor $\boldsymbol{G}_B(\mathbf{r}, \mathbf{r}')$ [60]. This procedure enforces a realistic no-slip boundary condition (BC) at the electrode surface ($z = 0$), yielding a fluid velocity,

$$\mathbf{v}_0(\mathbf{r}) = \int_{V'} \boldsymbol{G}_B(\mathbf{r}, \mathbf{r}')\, \mathbf{f}_{\text{slip}}(\mathbf{r}')\, d\mathbf{r}' \tag{7}$$

which properly spreads over the unbounded domain. In our discrete particle formulation, the force density $\mathbf{f}_{\text{slip}}$ is modeled by assigning forces $\mathbf{F}^{\text{slip}}$ to each virtual "slip" particle distributed along the Debye layer (orange blobs in Figure 1C). More precisely, $f_{\text{slip}}(\mathbf{r}) = \sum_i S(\mathbf{r} - \mathbf{R}_i^{\text{slip}})\mathbf{F}_i^{\text{slip}}$ where $\mathbf{F}_i^{\text{slip}}$ is the "slip" force acting on the the $i^{th}$ virtual particle and $S(\mathbf{r})$ is a localized Gaussian distribution function (kernel) similar to those used in the immersed boundary method (IBM) [61, 62]. These forces $\mathbf{F}_i^{\text{slip}}$ are thus spread to the fluid (in Equation (7)) to generate the electro-kinetic velocity field $\mathbf{v}_0(\mathbf{r})$, which is then interpolated at each NP location $\mathbf{R}$ to obtain $\mathbf{v}_0(\mathbf{R})$ in Equation (1). As explained in Section S8, spreading and interpolation operations acting on the Green's function $\boldsymbol{G}_B(\mathbf{r}, \mathbf{r}')$ lead to the corresponding mobility tensor $\boldsymbol{\mathcal{M}}$ and to the discrete (particle) version of Equation (7),[2]

$$\mathbf{v}_0(\mathbf{R}_i) = \sum_{j \in \text{slip}} \boldsymbol{\mathcal{M}}(\mathbf{R}_i, \mathbf{R}_j^{\text{slip}})\, \mathbf{F}_j^{\text{slip}} \tag{8}$$

where the sum extends over all the *virtual* (slip) particles creating the EK flow. The forces $\mathbf{F}^{\text{slip}}$ imposed to the virtual particles creating the EK flow are determined by enforcing their slip velocity given by Equation (6) following a hydrodynamically self-consistent way. This leads to a linear system of equations relating the (known) velocities $\mathbf{v}_i^{\text{slip}}$ and the (unknown) forces $\mathbf{F}^{\text{slip}}$ at the slipping boundaries,

$$\mathbf{v}_i^{\text{slip}} = \sum_j \boldsymbol{\mathcal{M}}(\mathbf{R}_i^{\text{slip}}, \mathbf{R}_j^{\text{slip}})\, \mathbf{F}_j^{\text{slip}} \tag{9}$$

where $\mathbf{R}_i^{\text{slip}}$ and $\mathbf{R}_j^{\text{slip}}$ now correspond to "slip" virtual-particle locations. Note that the virtual-particle velocity $\mathbf{v}_i^{\text{slip}}$ is obtained by interpolating the right-hand side of Equation (6) at $\mathbf{R}_i^{\text{slip}}$. To that end we use 3-pt Peskin-type interpolation kernels [61, 62] on the grid used to solve the potential $\phi$. We solve Equation (9) to obtain $\mathbf{F}^{\text{slip}}$ using the GPU-accelerated library `libMobility` [53], which computes the mobility tensor $\boldsymbol{\mathcal{M}}$ for different geometries. Instead of explicitly inverting $\boldsymbol{\mathcal{M}}$ (prohibitively expensive for large systems), we employ a GMRES iterative solver [63], which only requires evaluating matrix-vector products of the form $\boldsymbol{\mathcal{M}}\mathbf{F}$, efficiently provided by `libMobility`. Note that by using the Blake mobility tensor [60] we guarantee a physically consistent model: this corresponds to a no-slip BC at the electrodes' surface and a slip velocity at the midpoint of the EDL (20 nm above the wall). The resulting fluid flow $\mathbf{v}_0(\mathbf{r})$ is visualized by using IBM kernels to evaluate the flow velocity at "tracer" nodes located in a 3D regular mesh (e.g. the gray blob in Figure 1C).

### 3.4 | Regime of Validity

The present work relies on assumptions which become increasingly invalid for smaller particles in confined geometries. Within the classical CM theory, the expression used for the DEP force (see Equation (4)) assumes that the particle is spherical, has uniform properties, and has a diameter smaller than the inhomogeneities in the electric field, but larger than the Debye length (thin EDL assumption). Following the Maxwell-Wagner approximation [64], we take into account the double layer by including the particle's surface conductance in the thin double layers. However, the MW thin double layer assumption becomes quantitatively incorrect for sub-100 nm particles [64]. Calculations [65] and experiments [66] suggest that, for NPs smaller than the Debye length, the CM factor determining the polarizability might be 1000 times larger than the classical prediction. This is attributed to polarization phenomena in the particle's hydration shell and in the EDL, corresponding to the breakdown of the continuum approximation. Nevertheless, under the weak-field hypothesis, even with a thick double layer and additional electrokinetic effects, the net velocity of the particle will be proportional to the gradient of the electric field squared ($\alpha\nabla|\mathbf{E}|^2$) [67, 68]. Thus, given a particle's apparent polarizability, the DEP force will have the same form used in



16136829, 2026, 58, Downloaded from https://onlinelibrary.wiley.com/doi/10.1002/smll.75129, Wiley Online Library on [10/11/2026]. See the Terms and Conditions (https://onlinelibrary.wiley.com/terms-and-conditions) on Wiley Online Library for rules of use; OA articles are governed by the applicable Creative Commons License

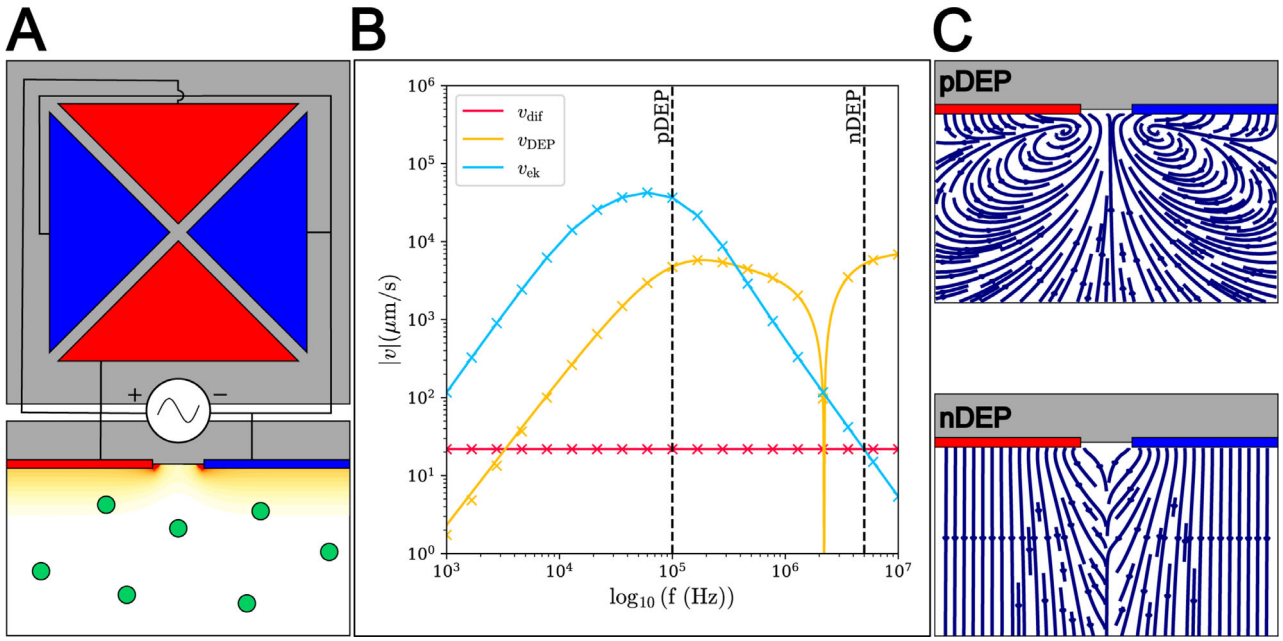



**Figure 3** | (A) Sketch of the quadrupole (top and side views). Red and blue colors represent a phase shift of $\pi$ between electrodes. Side view also includes contour plots of the normalized electric field intensity. Higher yellow color intensity indicates higher electric field intensity, showing that the highest intensity is at the edges of the electrodes. (B) The velocities associated to dielectrophoresis $v_{DEP} = \mu F_{DEP}$, AC electro-osmosis $v_{EK}$ and the characteristic diffusion velocity $v_{dif} = \mu kT/a$ with $\mu = (6\pi\eta a)^{-1}$ the NP mobility and $a$ the NP radius. These values are obtained from theoretical modeling, close to the gap between the electrodes. (C) Schematic representation of streamlines at both working frequencies. The top panel shows the combination of pDEP and electrokinetic flow and the bottom panel the streamlines expected for pure nDEP.

present approach [69], which remains valid in sufficiently dilute suspensions. In cases where particles present an asymmetric surface charge distribution or a permanent dipole, its time-averaged orientation with respect to the external field will affect the effective dipole moment, and the thermal average will depend on the particle rotational (Brownian) diffusivity. Additionally, the typically large surface charges found on polymeric particles may also induce local electrokinetic flows near the particle's surface, resulting in concentration polarization electro-osmosis (CPEO) [70]. Finally, we neglect electrothermal currents and ion currents created around the NPs, based on the expected scaling of these forces compared to DEP and electro-osmosis [56] (scaling laws and order of magnitude can be found in the Section S10).

## 4 | Results and Discussion

### 4.1 | Modeling Results

The outcome of the theoretical analysis is summarized in Figure 3. Figure 3B compares the velocities associated with the three main transport mechanisms: dielectrophoresis $\mathbf{v}_{DEP}(\mathbf{r}) = \mu F_{DEP}(\mathbf{r})$, EK flow $\mathbf{v}_{EK}(\mathbf{r})$ (both evaluated at a distance $z = 100$ nm from the electrode surface) and diffusion. To compare the first two with the thermal noise, we define the diffusion velocity $v_{dif} = \mu k_B T/a$ by calculating the time it would take for a particle to diffuse a mean square displacement equal to the squared half radius of the particle $a^2/4$.

To compute $f_{CM}$ with Equation (5) we need to know the complex permittivities of both particle and medium. The real part of the relative permittivity is $\varepsilon_m \approx 78.5$ for the solvent (water) and $\varepsilon_p \approx 2.5$ for the NPs (PS). For these values, one obtains a purely dielectric response at high frequencies, yielding nDEP with $f_{CM} \approx -0.5$. By contrast, conductivity transport, determined by $\sigma$, dominates at low frequencies. Therefore, there exists an intermediate cross-over frequency $\omega_{cr}$ at which $f_{CM}(\omega_{cr}) = 0$ (and $v_{DEP}(\omega_{cr}) = 0$, see Figure 3B). If $\varepsilon_m > \varepsilon_p$, a condition for obtaining pDEP at low frequencies is that $\sigma_p > \sigma_m$, however, the conductivity of water at 0.1 mM KCl ($\sigma_m = 0.0015$ S/m) is much higher than the electrical conductivity of polystyrene ($\sim 10^{-20}$ S/m), which would lead to nDEP throughout for any frequency. Nevertheless, we know from screening experiments that the carboxylate-modified polystyrene NPs exhibit pDEP at low frequencies and that the cross-over frequency lies in $\omega_{cr} \in [2.3 - 2.4]$ MHz (Figure 3B). This indicates a significant increase of $\sigma_p$ due to the additional contribution from ion conduction across the EDL shell surrounding the NP. A value of $\sigma_p \approx 0.013$ S/m is consistent with the experimentally observed $\omega_{cr}$ and agrees with the theoretical calculations reported by H. Zhao et al. [71] for a particle of 108 nm with bulk conductivity $\sigma_m = 0.0015$. Therefore, we use $\sigma_p = 0.013$ S/m in our calculations. The vertical dashed lines in Figure 3B indicate the frequencies used in our experiments, showing pDEP at 100 kHz and nDEP at 5 MHz. Note that EK flow is dominant at low frequencies and negligible at high frequencies. In particular, at high frequencies the EK velocity becomes smaller than the "Brownian velocity" $v_{dif} = \mu kT/a \approx 20\,\mu$m/s (although it is important to recall that the average Brownian velocity is zero, whereas EK flow represents a systematic drift). When the EK flow is very small $\mathbf{v}_0 \approx 0$, the steady-state NP density is close to the equilibrium distribution associated with the DEP potential,

$$P_{st} \approx P_{eq} \propto \exp(-\beta U_{DEP}) \tag{10}$$



16136829, 2026, 58, Downloaded from https://onlinelibrary.wiley.com/doi/10.1002/smll.75129, Wiley Online Library on [10/11/2026]. See the Terms and Conditions (https://onlinelibrary.wiley.com/terms-and-conditions) on Wiley Online Library for rules of use; OA articles are governed by the applicable Creative Commons License

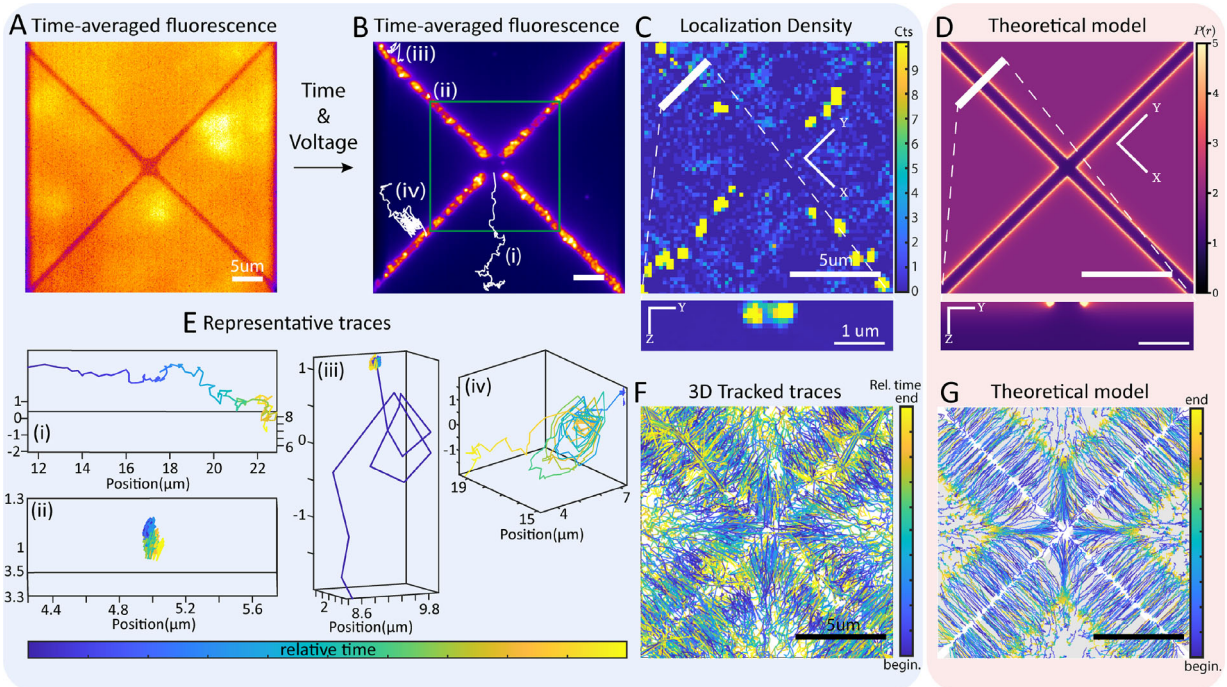



**Figure 4** | Experimental and theoretical analysis of pDEP. (A) Time-averaged image in the absence of any voltage showing a homogeneous intensity distribution. (B) Time-averaged image under 100 kHz and 0.75 V (amplitude) AC field showing preferential location of particles inside the electrode gap where the electric field gradient is strongest. (C) Localization density at the electrode combining data from multiple periods of 10 seconds exposure to 100 kHz at 0.5 V (pDEP). Color scale is logarithmic. The upper panel shows the XY view, while the lower panel shows a section of the ZY plane. (D) Theoretical NP equilibrium distribution $P_{eq} \sim \exp[-\beta U_{\mathrm{DEP}}]$ under pDEP (arbitrary units). Lighter colors correspond to higher $P_{eq}$. The upper panel displays the transverse XY plane located 50 nm above the electrode plane, while the lower panel shows a section of the ZY plane. (E) Representative 3D traces of different types of typical behavior: (i) ejection from center at 45 degrees w.r.t. the electrode arm, (ii) trapping at the electrode, (iii) moving from bulk solution to electrode gap, and (iv) escape from the trap, moving perpendicular to the electrode arm entering a vortex flow. Time color-code is given relatively for clarity (for each particle, the beginning of its trace is depicted in blue, while later times are depicted in yellow). (F) Top view of all the trajectories showing an overview of the characteristic behavior, notably ejection from the quadrupole center at 45 degrees from the electrode arms and ejection perpendicular to the electrode arm. (G) Top view of all the traces from the theoretical dynamical simulation showing the predicted behavior in a good match with experimental results.

Figure 3C shows theoretical trajectories of the studied NPs at both operating frequencies. At 100 kHz, the particles experience pDEP, and the EK flow is very intense. DEP pulls particles toward the electrode edges, while the EK flow generates two counter-rotating vortices along the dielectric corridor. The total motion results from the combination of both effects. In contrast, at 5 MHz NPs experience nDEP and the EK flow is much weaker (below the level of thermal noise). DEP pushes the NPs away from the electrodes and to the region where thermal noise dominates, where NPs are expected to move randomly.

## 4.2 | Positive DEP

### 4.2.1 | Localization Density, 3D Tracking and Theoretical View

We start by analyzing the experimental results for pDEP at 100kHz and 0.5$V$. Figure 4 details the results of pDEP from both the experimental and the theoretical point of view. Figure 4A shows the average intensity distribution of a 10 s movie without applied voltage. The intensity distribution is more or less uniform due to the random Brownian motion of the particles. Figure 4B also shows the average intensity distribution of a 10 s movie, but after applying pDEP frequency, demonstrating a clear accumulation of particles in the electrode gaps. This is expected because the region near the electrode is where the electric field intensity (and consequently $U_{\mathrm{DEP}}$) is highest.

To compare with theory, we looked at the experimental localization density (histogram) of the electrode plane Figure 4C which clearly shows that particles are predominantly attracted to and confined within the gap between electrodes (bright yellow spots), close to the electrode edges. Similarly, the probability density associated with the DEP potential Equation (10), shown in Figure 4D), has a strong maximum at the edges of the electrodes, suggesting an accumulation of particles (yellow strips in Figure 4B). While the effective "equilibrium" distribution associated to the DEP potential Equation (10) offers a good insight about the expected particle distribution, it should be noted that it is not strictly equal to the steady-state distribution $P_{st}$ of moving particles. A slight difference between the prediction from $P_{\mathrm{eq}}$ and the experiment is that in the experiment the particles seem to be more evenly distributed in the electrode gaps, in the XY view whereas $P_{\mathrm{eq}}$ is higher at the edges. However, the ZY view clearly shows the appearance of two localization density spots around 500–600 nm away from each other, just slightly below the electrode corridor width. To confirm this, we performed



16136829, 2026, 58, Downloaded from https://onlinelibrary.wiley.com/doi/10.1002/smll.75129, Wiley Online Library on [10/11/2026]. See the Terms and Conditions (https://onlinelibrary.wiley.com/terms-and-conditions) on Wiley Online Library for rules of use; OA articles are governed by the applicable Creative Commons License

pDEP experiments trapping smaller particles (63 nm diameter) which nicely showed that the accumulation is really taking place at the electrode edge, rather than distributed over the corridor (Figure S4).

To fully capture the details of NP dynamics we looked at individual trajectories in 3D. The analysis workflow can be found in Supplementary Note V. Figure 4E presents representative traces of particle trajectories during pDEP. These traces are color-coded for relative time, with blue representing the earlier part of the trace and yellow the later part. Figure 4E(i) presents a trace that is ejected away from the quadrupole center at 45 degrees from the electrode arms. Figure 4E(ii) shows a trace of a particle trapped in the electrode gap. Figure 4E(iii) shows a particle going from the bulk solution to the electrode, with a loop motion on the way. Figure 4E(iv) shows a particle that was initially trapped, then released, likely due to local flow, and was then stuck in a vortex loop before escaping. This vortex motion and ejection is perpendicular to the electrode arm. Additional trace examples for these different types of motions can be found in Section S6.

Figure 4F shows a top view of all the particles tracked on all 10 movies using the same relative time color-coding. Similarly to the individual traces extracted before, we observe several areas exhibiting different particle dynamics. Inside the corridors, a high concentration of yellow traces confirms particle capture in the region of high electric field strength, close to the electrodes. Secondly, perpendicular to the corridors of the electrode cross, particles appear to be ejected, as traces transition from blue near the electrode to yellow further away (corresponding to observation at shorter time close to electrode and at longer time away from electrode). This was found later to be associated to vortex-like flows (see details in next section). Finally, we observed that particles are expelled from the electrode center in four directions at 45° angles with respect to the cross formed by the corridors. This effect, also captured by modeling, was found to be stronger at higher voltage; see Figure S6.

These experimentally observed dynamics agree well with the theoretically predicted behavior. Figure 4G shows the simulated trajectories of 2000 NPs under equivalent DEP and EK flow conditions. The color code is the same as in Figure 4F, to facilitate comparison with experiment. We solved the dynamics using the multiphysics software `UAMMD-structured` [55, 61], which includes a Brownian dynamics solver and allows the user to include an external tabulated force field in the simulation. This force field incorporates the contributions of both effects included in our model. The results show that particles approach the electrode's gap due to DEP, and some of them are ejected by EK flows perpendicular to the electrode arms, resulting in a picture that is fully consistent with the experimental observations.

#### 4.2.2 | 3D Flow Visualization and Speed Profiles

Building on the previous section, we use the tracked traces to map the speed of particles in the three-dimensional (3D) space and compare these velocities with theoretical calculations. Figure 5 shows the particle motion in a cross-section perpendicular to the electrode gap. The aforementioned ejection perpendicular to the electrode in Figure 4F is part of a more complex vortical motion in 3D. Given the axial direction of the vortex, this could not have been observed easily with a standard microscope. Theory and modeling reveals that the ejection normal to the electrode corridors is driven by AC electro-osmosis,. This EK flow forms two counter-rotating vortices (Figures 3C and 5) unfolding in the normal planes of the inter-electrode corridors; expelling particles to the bulk on both sides while gathering particles from the bulk in its central domain. Close to the electrode corridors the attractive DEP force becomes significantly large, but it soon decreases as the NPs move away from the electrode surface.

Figure 5 compares theoretical and experimental 3D reconstruction of these vortical trajectories. Indeed, an excellent agreement is found both in the vortex dimensions (each one about 2.5 microns in size) and in the typical velocities attained (Figure 5C). Theory predicts the largest velocities to be at a layer of less than 1 micron adjacent to the electrodes. These velocities are however too high to allow for experimental observation. Away from this layer (i.e., about 1 micron away from the electrode surface) experiments and theory quantitatively agree well on particle speeds, ranging from $\sim 100\,\mu$m/s close to the electrodes to $\sim 30\,\mu$m/s a further 4 microns away[3].

Close to the electrode centre, EK vortices coming from different electrode arms merge to create two counter-rotating pairs of larger ejecting vortices, tilted 45° with respect the corridor directions. This leads to an increase in tracked NPs in these orthogonal directions, which is not immediately apparent from the trajectories using 0.5 V in 4C, but becomes very clear if the voltage is increased to 0.75 V (Figure S6).

As explained above, the theoretical velocity field is measured on a regular 3D mesh of cells. To obtain an experimental velocity field amenable for comparison with the theoretical prediction, we measured the experimental velocities of all detected NPs at various times by calculating their displacements between two consecutive time-frames. We then averaged these velocities within regular cells of side 500 nm. Figure 5A,C shows 2D representations of these fields, obtained by averaging along the corridor (normal) direction. These 2D streamlines are calculated using the basic streamplot function in matplotlib in Python. Figure 5B,D shows 3D representations obtained with the `PyVista` [54] software, allowing us to see the full 3D motion. Clearer and interactive 3D renderings of these complex flows are available at https://padisi.github.io/quadrupole-paper/. Figure 5 shows an excellent match between experimental and theoretical particle flow. Minor mismatches can reasonably be attributed to experimental limitations. In particular, inside the zone indicated in red in Figure 5, the experimental evaluation of the velocities is inaccurate due to the high speeds $v > 100\mu\text{m}/s$ and the small distance $\ell$ to the geometrical barrier of the surface (such that $\ell < v\Delta t_{sample}$). Yet, the combined results from experiment and model qualitatively and quantitatively capture the complexity of the colloidal dynamics in 3D.

### 4.3 | Negative DEP

Now we turn our attention to the dynamics under typical nDEP conditions. Figures 6 and 7 show results obtained for 5 MHz



16136829, 2026, 58, Downloaded from https://onlinelibrary.wiley.com/doi/10.1002/smll.75129, Wiley Online Library on [10/11/2026]. See the Terms and Conditions (https://onlinelibrary.wiley.com/terms-and-conditions) on Wiley Online Library for rules of use; OA articles are governed by the applicable Creative Commons License

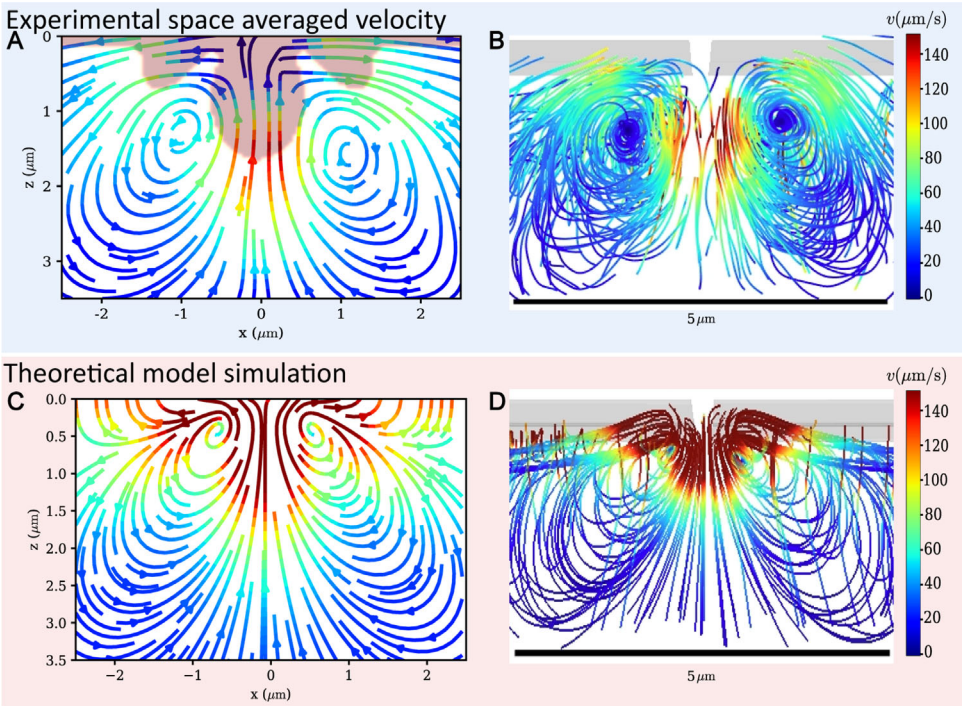



**Figure 5** | Comparison of experimental and theoretical velocity fields averaged over the corridor direction. Fully 3D and interactive images illustrating trajectories and velocity fields derived from experiments and simulations are available at https://padisi.github.io/quadrupole-paper/. The red transparent zone overlaid with the experimental figure indicates where theoretical predicted velocity is higher than 110 $\mu$m/s and proximity to the surface, resulting in inaccurate experimentally recovered velocities. (A) Experimentally measured velocity streamlines averaged along the corridor. (B) Three-dimensional visualization of the experimentally measured velocity streamlines viewed from within the corridor. (C) Theoretically calculated velocity streamlines averaged along the corridor. (D) Three-dimensional visualization of the theoretically calculated velocity streamlines viewed from the corridor.

and 1 V. Compared to pDEP, the experimental observation of nDEP dynamics is much more challenging as it strongly repels particles from the electrode region toward the bulk. Moreover, electro-osmotic flows at these high frequencies are weak, so other types of driving mechanisms not included in the model become increasingly relevant [36].

We first describe the expected behavior of the NPs according to our model, which includes both DEP and EK effects. The Boltzmann distribution $P_{eq}$ associated to the DEP potential increases away from the electrodes, reaching a plateau in the bulk, at distances $\sim 1\,\mu$m below the electrodes. This means that most NP should be located in the bulk, while close to the electrodes a depletion layer forms with a width of about 0.25 $\mu$m. Figure 6D shows the structure of $P_{eq}$ in a ZX section, showing the depleted layer adjacent to the electrodes. The inset in Figure 6D indicates $P_{eq}$ in the XY plane, very close to the electrodes (50 nm). Note that, as the field vanishes at the center line of the electrode gaps, the gaps appear to have larger $P_{eq}$ than the immediate surroundings. However, this is misleading: very few or no particles reach the inter-gap domain close to the electrodes and indeed, very long times would be required to sample those rare events. Consistent with this observation, the theoretical net velocity field (DEP+EK) in Figure 7C,D clearly indicates a strong ejection from the electrodes ($z = 0$ plane) toward the bulk. The high-velocity layer extending up to $\sim$ 0.25$\mu$m indicates the depleted domain. Still from the theoretical perspective, the EK flow dominates in the bulk, leading to vortical structures (curved trajectories in Figure 7C,D). However, at the bulk, the EK velocity is much smaller than the Brownian velocity $v_0 \ll v_{\text{dif}} \approx 20\,\mu$m/s, implying that the EK flow would be difficult to detect or sample experimentally. As expected, Figure 6G shows that the NP trajectories calculated from Equation (1) and the theoretical fields are basically random upon reaching the bulk after expulsion.

Experimental results confirm the theoretical prediction (Figure 7C) concerning the formation of a depletion layer close to the electrodes of about 150–300 nm, and a bulk region dominated by Brownian displacements. However, a closer inspection revealed several interesting patterns not predicted by the theory. Figure 6A shows the average intensity distribution of a 10 s movie without applied voltage. As expected, the intensity distribution is homogeneous, corresponding to Brownian motion of the fluorescent NPs. In contrast, Figure 6B shows the time-averaged fluorescence of the same region after applying the selected nDEP condition (1 V, 5 MHz), revealing an unexpected accumulation of particles at distances of $\sim [0.2 - 0.3]\,\mu$m *below* the electrode edges (the determination of this height is described in Figure S9), moving along the borders of the depleted layers. The trajectories of individual representative particles (Figure 6E) reveal further information. Representative traces highlight four main observed behaviors: (i) Particles sliding along the electrode edges, approximately 0.25 $\mu$m below the electrode plane. (ii) Particles moving from the bulk solution and subsequently sliding along the corridor in a manner similar to (i). (iii) Particles moving from the bulk to the electrode



16136829, 2026, 58, Downloaded from https://onlinelibrary.wiley.com/doi/10.1002/smll.75129, Wiley Online Library on [10/11/2026]. See the Terms and Conditions (https://onlinelibrary.wiley.com/terms-and-conditions) on Wiley Online Library for rules of use; OA articles are governed by the applicable Creative Commons License

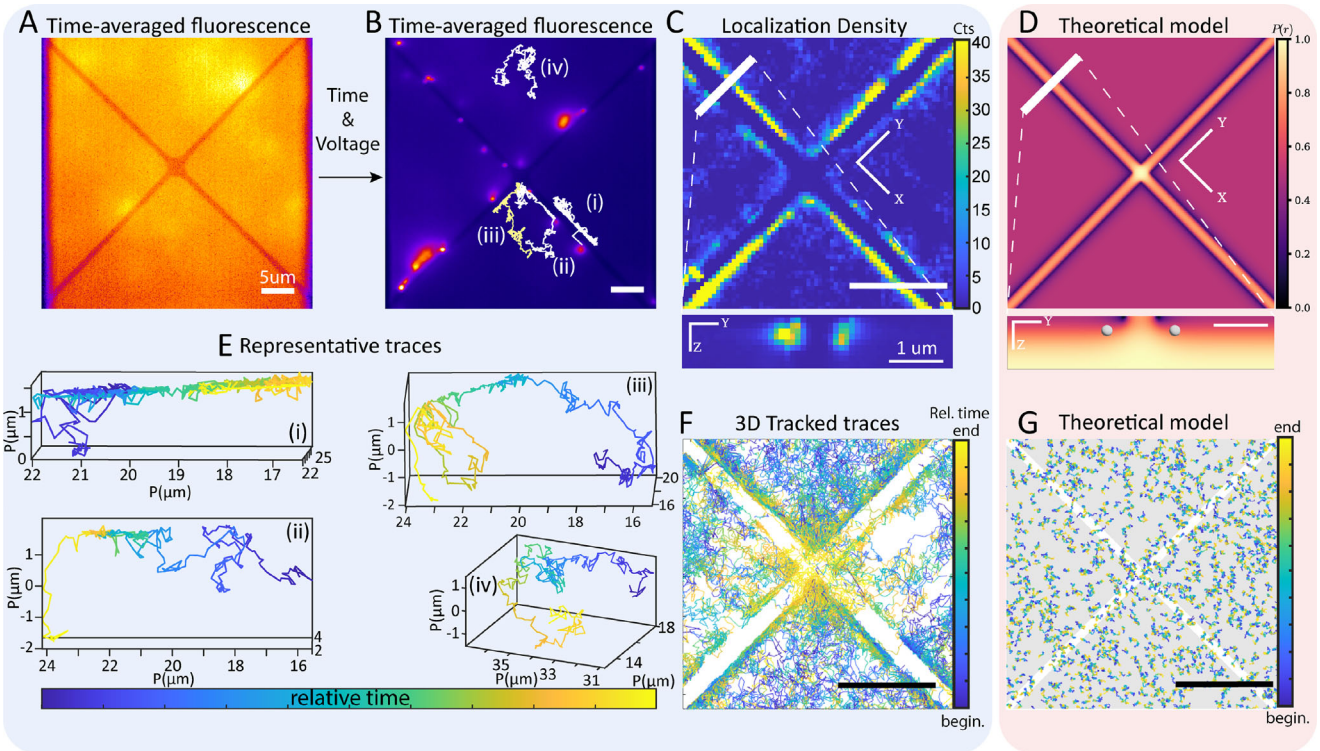



**Figure 6** | Experimental and theoretical analysis of nDEP. (A) Time-averaged image in the absence of an AC field, showing a homogeneous intensity distribution. (B) Time-averaged image under a 1 MHz and 1 V AC field, showing preferential location of particles just outside the electrode corridor. (C) Localization density at the electrode combining data from multiple cycles of 10 second exposure to 5 MHz at 1 V (nDEP). The upper panel shows the XY view, while the lower panel shows a section of the ZY plane. (D) Theoretical equilibrium probability distribution $P_{eq} \sim \exp(-\beta U_{\mathrm{DEP}})$ under nDEP (arbitrary units). Lighter colors correspond to higher $P_{eq}$. The upper panel presents $P_{eq}$ isocontours in the transverse XY plane located 50 nm above the electrodes. The lower panel displays the ZY plane centered at the electrode corridor. Cartoon particles are depicted at the locations of experimentally observed NP flow along the electrode arm, corresponding to the yellow regions in (C). (E) Representative 3D traces of different typical behavior: (i) movement along electrode corridor, moving at about 500 nm above the electrode edge, (ii) full cycle, moving from bulk solution to horizontal movement above the electrode gap, and finally repulsion in a vortex toward the bulk after reaching the center of the quadrupole, (iii) shows similar behavior as (ii) but is expelled more vertically, and (iv) shows Brownian motion in the bulk. Time color-code is given relatively for clarity (for each particle, the beginning of its trace is depicted in blue, while later times are depicted in yellow). (F) Top view of all the detected traces gives an overall view of the the characteristic behaviors, notably the absence of particles inside the gap between the electrodes and the attraction toward the center of the quadrupole. (G) Top view of all the traces from the theoretical dynamical simulation showing the predicted behavior, which mostly corresponds to particle being pushed away from the electrodes and subsequent random, diffusion-dominated motion.

corridor and being repelled at the center of the quadrupole downward to the bulk, resulting in a looping motion. (iv) Pure Brownian motion, as in fact, many particles do not appear to experience any significant drift force.

Another remarkable observation is the presence of two counter-rotating vortices (Figure 7A) localized around the quadrupole center. As clearly shown in the interactive 3D flow-map https://padisi.github.io/quadrupole-paper/ , the vortex plane is tilted 45° with respect the quadrupole corridors with vorticity vector-field mainly along Y-direction and vortex plane in XZ (Figure 7B). The sense of rotation of these vortices is opposite to the EK vortices discussed in the pDEP section. In particular, just below the electrodes, these new vortices (Figure 7A) eject NPs away toward the bulk; while we recall that in pDEP, EK vortices (commonly referred to as sweep vortices) sweep or attract NPs toward the electrodes (Figure 5). Overall, Figure 7A clearly illustrates the high-velocity, depleted domain, with a layer of about 150 nm devoid of any particle trace, in agreement with the theoretical nDEP prediction (Figure 7C). However, the observed pair of counter-rotating vortices close to the quadrupole center is not predicted by the theory.

In summary, experiments at nDEP condition revealed flows that are not explained by our current model; notably the accumulation of NPs below the electrode edges and the ejecting counter-rotating vortices at the quadrupole center. This type of accumulation is typically due to counteracting effects [72]. We observed accumulation at a $\sim 0.2 - 0.3\,\mu$m vertical distance from the electrodes, where DEP and EK (electro-osmosis) are rather weak. These small flows might be of electrothermal origin and/or due to electrolyte currents formed around the NPs which might interact with the walls. Electrothermal driving is a plausible candidate for the vortex pair, as they are formed just close to the quadrupole center, precisely where the intensity of the electric field is largest, and are observed at high frequencies [56]. While further analysis is required to draw firm conclusions, the present experimental results highlight the value of the 3D microscopy



16136829, 2026, 58, Downloaded from https://onlinelibrary.wiley.com/doi/10.1002/smll.75129, Wiley Online Library on [10/11/2026]. See the Terms and Conditions (https://onlinelibrary.wiley.com/terms-and-conditions) on Wiley Online Library for rules of use; OA articles are governed by the applicable Creative Commons License

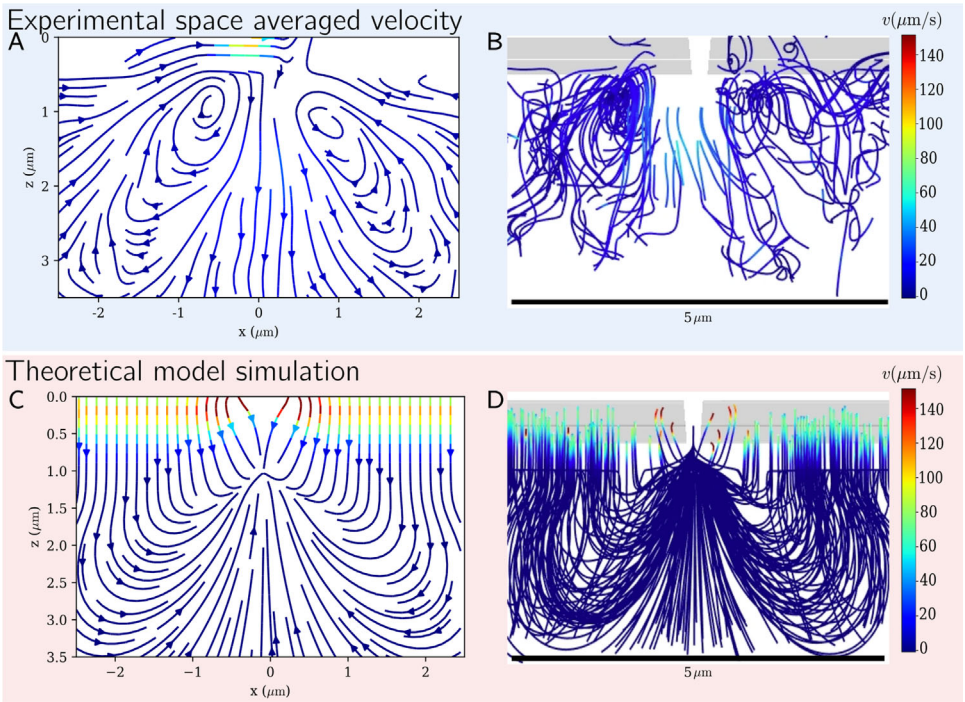



**Figure 7** | Comparison of 3D flows in nDEP observed by experiment and predicted by theory. (A) Streamline calculated from spatially averaged velocities in a cross-section taken perpendicular to the electrode corridor. (B) 3D view of the streamline. (C) Theoretical model of nDEP force and electrokinetic flow, projected on the same axis as panel A. (D) 3D representation of the calculated flow lines in nDEP. For a full 3D interactive view of the vortex pair shown in (A) and (B) click on https://padisi.github.io/quadrupole-paper/ and select `nDEP, Speed, Experiment`.

technique presented in this work, offering a unique tool to detect small and localized 3D NP-flow patterns under rather strong noise conditions.

## 5 | Conclusions

We presented a combined 3D mapping and computational simulation of the time-dependent flow and velocity field of NPs under pDEP and nDEP conditions. MPM was used for the first time to for fast imaging of colloidal electrokinetics in 3D, and successfully revealed the complicated NP dynamics close to a quadrupolar electrode generating an AC field. This complexity is due to the combined effect of electrokinetics, DEP and particle diffusion. We also introduced a novel theoretical approach, which models the ion-induced slip EK flow by using immersed-boundary virtual particles as boundary-force generators. This allows for the direct modeling of the 3D trajectories. For pDEP the excellent match between experimental and modeled trajectories shows the current theory captures the behavior of the 200 nm PS spheres very well. In short, pDEP mainly attracts particles to the electrode edges, inside the corridor between the electrodes. But at the same time, the EK flow created at the double layer expels some NPs in the normal direction to the corridors, mostly parallel to their plane. Just by fluid continuity, this leads to a flow pattern with circular trajectories following the vortical structures created near the gaps. These become stronger and even merge as the voltage is increased, creating extra orthogonal vortices (in the $x = 0$ and $y = 0$ planes, Figure S5). While in pDEP, theoretical modeling correctly recovers all these complex features, in nDEP we find subtle discrepancies with experiments. Theory would predict a strong repulsion from the surface and then Brownian motion in the bulk. Experimentally we indeed see that particles are repelled from the high-field domains in the electrodes gaps, resulting in a highly depleted layer of about 0.25 microns close to the electrodes, but the 3D tracking reveals that the NPs are driven toward the adjacent domain (about 0.25 micron deep in the solution) and some of them tend to gather there. These "trapped" particles then experience a mild driving force toward the electrode centre, floating above the electrode edge. At the center, they form a pair of ejecting vortices. While the theoretical model (incorporating DEP and EK flows) predicts the depletion layer, it does not reproduce the intermediate layer and the localized central ejecting vortices. Our observations appear different from an earlier report on levitation in a dielectrophoretic regime [73]. The observed central ejecting vortex is probably due to electrothermal effects (larger close to the quadrupole center) while the mild driving force could be due to particle-induced EK flows, which may hydrodynamically interact with the wall creating a net driving momentum. These observations advocate for the use of this integrated experimental/theoretical method, as on one hand we show that pDEP is very well understood at this scale, while a complete understanding of these complex flows in nDEP will require further refinement of our multiscale-multiphysics models, keeping quantitative connection with fast 3D multiplane microscopy imaging. Due to the complexity of these multiscale flows (ranging from boundary-layers of nanometers-size to vortical flows of hundred of micrometers), such a quantitative match demands the unprecedented level of detail and 3D perspective attainable with the presented experimental approach. Building on this approach, our goal is to offer valuable insights for future applications in NP manipulation and assembly. We expect to



16136829, 2026, 58, Downloaded from https://onlinelibrary.wiley.com/doi/10.1002/smll.75129, Wiley Online Library on [10/11/2026]. See the Terms and Conditions (https://onlinelibrary.wiley.com/terms-and-conditions) on Wiley Online Library for rules of use; OA articles are governed by the applicable Creative Commons License

be able to measure the particle polarizability under different conditions, elucidate the details of particle-induced EK-flows and the hydrodynamic interaction with other NPs and the wall-induced EK-flows, which become relevant in dense suspensions, as well as averaged magnetic dipolar interactions. Importantly, the present method is highly promising for the study of sub-100 nm particles, where the assumptions inherent in the NPs polarizability equations might no longer be valid. A first proof of concept of the feasibility was provided by imaging 63 nm particles. In conclusion, we have provided a comprehensive experiment and modeling framework to study NP manipulation and flows, adaptable to any electrode geometry and broadly applicable to colloidal systems in general.

## 6 | Materials and Methods

### 6.1 | Multiplane Widefield Microscope

All experiments have been performed using a multiplane widefield microscope (Figure 1) Briefly, a 488 or 561 nm laser line was used as widefield photo-excitation source by focusing it at the back focal plane of a water-immersion objective lens (N.A. = 1.20, 60x, Olympus UplanSApo60XW). The fluorescence emission was collected by the same objective lens and filtered with the suitable optical filter(s) to remove the widefield excitation laser and the emission of the unwanted fluorescent NPs. Afterward, the emitted light went through a set of lenses in telecentric 4f configuration [Objective - Lens1 – field stop - Lens2 - Tube lens – Camera(s)]. The field stop was used to control the size of the image. Between the tube lens and the cameras, we placed a proprietary prism, which split the entering photon flux into eight different beams with slightly different optical path lengths. The distance between consecutive planes is roughly 580 nm, yielding an axial range of approximately 4 $\mu$m. The different imaging planes were recorded by 2 CMOS cameras (4 imaging planes for each camera, Orca Flash 4.0, Hamamatsu Photonics Inc.). To ensure fast acquisition rates (100 fps) and correct synchronization of the two CMOS cameras, we triggered the acquisition via a National Instruments board (NI, USB-6343) coupled to a home-built software written in Labview. The imaging volume was 400 pixels × 400 pixels × 8 planes ($40 \times 40 \times 4\ \mu m^3$).

### 6.2 | Sample Preparation for Microscopy

Since the MPM is an inverted microscope, we used a circular spacer (Grace Bio-Labs SecureSeal imaging spacer, diameter 9 mm, thickness 0.12 mm) to create a small sample chamber on the surface of the chip, which holds about 8 $\mu$L of sample solution, and is closed off with a 0.15 mm cover glass. Commercially available fluorescently labeled carboxylate polystyrene (PS) FluoSpheres Carboxylate-Modified Microspheres yellow-green (200 nm Thermo Fisher) were diluted 10 mM MES buffer solution (pH 6), enabling control of surface charges and ionic strength. The procedure to prepare the buffer was as follows: 1.952 g MES (2-(N-morpholino)ethanesulfonic acid) free acid was dissolved in 800 mL deionized water. 0.442 g KCl was added to fix the ionic strength at 10 mM. Then the final volume of the solution was adjusted to 1000 mL with deionized water. Then the solution was titrated to pH 5.99 with monovalent strong base or acid as needed.

### 6.3 | Single Particle Tracking (SPT) Analysis

To track the motion of the NPs we used a house-written algorithm. The detail of the algorithm used for detecting and tracking the NPs is described elsewhere [51]. Briefly, each NP is detected on different planes and then localized in 3D. After calculating the (x-, y-, z-) coordinates of each single emitter in the time-lapse image sequence, they were connected in time to form trajectories. The correspondence assignment was performed by minimizing the sum of the displacements of all NPs via Munkres algorithm. Both localization and tracking algorithms are freely available at https://github.com/BorisLouis/3D-image-processing.

Other analysis and post processing are described in Section S5.

### 6.4 | Device Processing

The polynomial design, known as quadrupole, is fabricated using the standard silicon processing techniques. Initially, the 1000 nm silicon oxide was deposited on the p-type 300 mm silicon wafer as electrical isolation layer and to reduce capacitive coupling with the substrate. This was followed by the deposition of a 2 nm TaN (ALD) and 50 nm ruthenium (PVD) metal layer. The electrode shape was further processed on this metal layer with lithography patterning and dry etching. Next, a 20 nm silicon nitride layer was deposited, followed by the deposition of a 50 nm silicon oxide. Finally, further etching was performed to expose the Ru metal layer. The center separation of the quadruple is 2 $\mu$m. The design generates a steep electric field gradients at the tips and edges, while simultaneously generating a steep electric field that points toward low electric field at the center of the quadrupole.

### 6.5 | Nanoparticle Preparation

Poly(methyl methacrylate-co-methacrylic acid) nanoparticles loaded with rhodamine were prepared as previously reported [74] using the following procedure. Stock solutions of PMMA-MA in acetonitrile were prepared at a concentration of $10 mg mL^{-1}$. This solution was then diluted with acetonitrile to $2\ mgmL^{-1}$ with 30% (w/w) of R18/5F-TPB relative to the polymer. 50 $\mu$L of the polymer solution were then added quickly using a micropipette and under shaking (Thermomixer Comfort, Eppendorf, 900 rpm) to 450 $\mu$L of phosphate buffer (20 mM, pH 7.4) at room temperature. The nanoparticle solution was then quickly diluted fivefold with the same buffer.

### 6.6 | Nanoparticle Characterization (Dynamic Light Scattering)

Measurements for the determination of the size distribution of the nanoparticles were performed on a Zetasizer Nano series DTS 1060 (Malvern Instruments S.A.). The mean value of the diameter of the size distribution per volume was used for analysis.



16136829, 2026, 58, Downloaded from https://onlinelibrary.wiley.com/doi/10.1002/smll.75129, Wiley Online Library on [10/11/2026]. See the Terms and Conditions (https://onlinelibrary.wiley.com/terms-and-conditions) on Wiley Online Library for rules of use; OA articles are governed by the applicable Creative Commons License

## Acknowledgments

This work was funded by the European Union under the Horizon Europe grant 101130615 (FASTCOMET). Views and opinions expressed are however those of the author(s) only and do not necessarily reflect those of the European Union or the European Innovation Council and SMEs Executive Agency. Neither the European Union nor the granting authority can be held responsible for them. This work was also supported by the Flemish Government through long term structural funding Methusalem (CASAS2, Meth/15/04), by the Fonds voor Wetenschappelijk Onderzoek-Vlaanderen (FWO, G046126N, W002221N), by a bilateral agreement between FWO and MOST (VS00721N), by the internal funds of KU Leuven (C14/22/085), by the Spanish Agencia Estatal de Investigación (AEI) and FEDER (PID2022-137569NA-C44, PID2022-137569NB-C43, PID2020-117080RB-C51 and PDC2021-121441-C21, CNS2025-166106, PID2025-169749NB-C32). S.S. acknowledges the support of Marie Skłodowska-Curie postdoctoral fellowship (No. 101151427, SPS_Nano) from the European Union's Horizon Europe program. B.L. acknowledges FWO for his junior postdoctoral fellowship (12AGZ24N). R.B.-O. thanks the Spanish Agencia Estatal de Investigación for a Ramon y Cajal contract (RYC2021-032773-I). M.I.M. acknowledges financial from the Spanish Ministry of Science and Innovation (MCIN), AEI, and the María de Maeztu Programme for Units of Excellence in R&D (CEX2023-001316-M). R.D-B and P.D.S acknowledge funding from Spanish AEI grant PID2024-158994OB-C41. The authors thank Imec's Industrial Affiliation Program on Storage Memory Devices for support in fabricating the chips.

## Conflicts of Interest

The authors declare no conflicts of interest.

## Data Availability Statement

The data that support the findings of this study are available from the corresponding author upon reasonable request.

## Endnotes

[1] As mentioned by Ramos et al. [58] it is also possible to use a generalized model with a minor resistance component

[2] A similar operation might be done to include the hydrodynamic coupling between real particles, although this minor contribution was neglected in Equation (1).

[3] Experimental speeds are comprised in the range of $[0 - 250]\ \mu$m/s with 95th percentile at 63 $\mu$m/s and a 99th percentile at 145 $\mu$m/s.

## References

1. P. Sajeesh and A. K. Sen, "Particle Separation and Sorting in Microfluidic Devices: A Review," *Microfluidics and Nanofluidics* 17, no. 1 (2014): 1–52.

2. H. Cha, L. Ouyang, X. Chen, et al., "Leveraging Dielectrophoresis in Inertial Flow for Versatile Manipulation of Micro and Nanoparticles," *Lab on a Chip* 25, no. 12 (June 2025): 2816–2827, https://doi.org/10.1039/d4lc01037j.

3. F. Fontana, E. Carollo, G. E. Melling, and D. R. F. Carter, "Extracellular Vesicles: Emerging Modulators of Cancer Drug Resistance," *Cancers* 13, no. 4 (2021): 749.

4. S. John, "Strong Localization of Photons in Certain Disordered Dielectric Superlattices," *Physical Review Letters* 58, no. 23 (1987): 2486–2489.

5. S. Zhang, Y. Wang, P. Onck, and J. Den Toonder, "A Concise Review of Microfluidic Particle Manipulation Methods," *Microfluidics and Nanofluidics* 24, no. 4 (2020): 24.

6. I. Rachbuch, S. Park, Y. Katz, T. Miloh, and G. Yossifon, "Hybrid Magnetic-Electric Actuation for Enhanced Motion Control and Multi-Surface Operation of Janus Microrobots," *Nature Communications* 17, no. 1 (May 2026): 5993, https://doi.org/10.1038/s41467-026-72408-6.

7. Q. Chen and Y. J. Yuan, "A Review of Polystyrene Bead Manipulation by Dielectrophoresis," *RSC Advances* 9, no. 9 (2019): 4963–4981.

8. T. Ghomian and J. Hihath, "Review of Dielectrophoretic Manipulation of Micro and Nanomaterials: Fundamentals, Recent Developments, and Challenges," *IEEE Transactions on Biomedical Engineering* 70, no. 1 (2023): 27–41.

9. J. Yao, K. Zhao, J. Lou, and K. Zhang, "Recent Advances in Dielectrophoretic Manipulation and Separation of Microparticles and Biological Cells," *Biosensors* 14, no. 9 (2024): 417.

10. N. N. N. Ahamed, C. A. Mendiola-Escobedo, O. D. Ernst, V. H. Perez-Gonzalez, and B. H. Lapizco-Encinas, "Fine-Tuning the Characteristics of the Applied Potential To Improve AC-iEK Separations of Microparticles," *Analytical Chemistry* 95, no. 26 (July 2023): 9914–9923, https://doi.org/10.1021/acs.analchem.3c00995.

11. M. Rosmeulen, C. J. L. de la Rosa, K. Willems, et al., "Liquid Memory and the Future of Data Storage," *2022 IEEE International Memory Workshop (IMW)* (2022): 1–4, https://api.semanticscholar.org/CorpusID:249048837.

12. B.-Y. Shih, S. Fransen, R. Tahvildari, et al., "Ultra-High Bit Density Liquid-State Colloidal Memory," *Memories - Materials, Devices, Circuits and Systems* 14 (2026): 100143, https://www.sciencedirect.com/science/article/pii/S277306462600006X.

13. J. H. Hannay, "The Clausius-Mossotti Equation: An Alternative Derivation," *European Journal of Physics* 4, no. 3 (1983): 141–143.

14. J. Regtmeier, T. T. Duong, R. Eichhorn, D. Anselmetti, and A. Ros, "Dielectrophoretic Manipulation of DNA: Separation and Polarizability," *Analytical Chemistry* 79, no. 10 (2007): 3925–3932.

15. M. Farasat, E. Aalaei, S. Kheirati Ronizi, et al., "Signal-Based Methods in Dielectrophoresis for Cell and Particle Separation," *Biosensors* 12, no. 7 (2022): 510.

16. I. Najafipour, P. Sadeh, A. M. Amani, et al., "Dielectrophoresis-Based Microfluidics for Detection and Separation of Circulating Tumor Cells," *Sensors and Actuators Reports* 9 (2025): 100304, https://www.sciencedirect.com/science/article/pii/S2666053925000232.

17. S. Valijam, A. Salehi, and M. Andersson, "Design of a Low-Voltage Dielectrophoresis Lab-on-the-Chip To Separate Tumor and Blood Cells," *Microfluidics and Nanofluidics* 27, no. 3 (Feb. 2023): 22, https://doi.org/10.1007/s10404-023-02632-9.

18. L. Yang, "A Review of Multifunctions of Dielectrophoresis in Biosensors and Biochips for Bacteria Detection," *Analytical Letters* 45, no. 2–3 (2012): 187–201.

19. B. H. Lapizco-Encinas and M. Rito-Palomares, "Dielectrophoresis for the Manipulation of Nanobioparticles," *Electrophoresis* 28, no. 24 (2007): 4521–4538.

20. M. Nakano, Z. Ding, and J. Suehiro, "Dielectrophoresis and Dielectrophoretic Impedance Detection of Adenovirus and Rotavirus," *Japanese Journal of Applied Physics* 55, no. 1 (2016): 017001.

21. B. C. Gierhart, D. G. Howitt, S. J. Chen, R. L. Smith, and S. D. Collins, "Frequency Dependence of Gold Nanoparticle Superassembly by Dielectrophoresis," *Langmuir* 23, no. 24 (2007): 12450–12456.

22. M. Duchamp, K. Lee, B. Dwir, et al., "Controlled Positioning of Carbon Nanotubes by Dielectrophoresis: Insights into the Solvent and Substrate Role," *ACS Nano* 4, no. 1 (2010): 279–284.

23. D.-J. Kim, J.-H. Hyung, D.-W. Seo, D.-I. Suh, and S.-K. Lee, "Dual-Gate Multiple-Channel ZnO Nanowire Transistors," *Journal of Electronic Materials* 39, no. 5 (2010): 563–567.

24. B. Sarno, D. Heineck, M. J. Heller, and S. D. Ibsen, "Dielectrophoresis: Developments and Applications from 2010 to 2020," *Electrophoresis* 42, no. 5 (2021): 539–564.

25. J. Suehiro, R. Yatsunami, R. Hamada, and M. Hara, "Quantitative Estimation of Biological Cell Concentration Suspended in Aqueous



16136829, 2026, 58, Downloaded from https://onlinelibrary.wiley.com/doi/10.1002/smll.75129, Wiley Online Library on [10/11/2026]. See the Terms and Conditions (https://onlinelibrary.wiley.com/terms-and-conditions) on Wiley Online Library for rules of use; OA articles are governed by the applicable Creative Commons License

Medium by Using Dielectrophoretic Impedance Measurement Method," *Journal of Physics D: Applied Physics* 32, no. 21 (1999): 2814.

26. J. Suehiro, M. Shutou, T. Hatano, and M. Hara, "High-Sensitive Detection of Biological Cells Using Dielectrophoretic Impedance Measurement Method Combined with Electropermeabilization," *Sensors and Actuators B: Chemical* 96, no. 1 (2003): 144–151.

27. R. Reale, A. Di Ninno, L. Businaro, P. Bisegna, and F. Caselli, "A Simple Electrical Approach To Monitor Dielectrophoretic Focusing of Particles Flowing in a Microchannel," *Electrophoresis* 40, no. 10 (2019): 1400–1407.

28. J. P. H. Burt, T. A. K. Al-Ameen, and R. Pethig, "An Optical Dielectrophoresis Spectrometer for Low-Frequency Measurements on Colloidal Suspensions," *Journal of Physics E: Scientific Instruments* 22, no. 11 (1989): 952.

29. M. S. Talary and R. Pethig, "Optical Technique for Measuring the Positive and Negative Dielectrophoretic Behaviour of Cells and Colloidal Suspensions," *IEE Proceedings - Science, Measurement and Technology* 141, no. 5 (1994): 395–399.

30. C. Midelet and M. H. V. Werts, "Dielectrophoretically Modulated Optical Spectroscopy of Colloidal Nanoparticle Solutions in Microfluidic Channels," *Particle & Particle Systems Characterization* 37, no. 10 (2020): 2000187.

31. V. E. Froude, J. I. Godfroy, S. Wang, H. Dombek, and Y. Zhu, "Anomalous Dielectrophoresis of Nanoparticles: A Rapid and Sensitive Characterization by Single-Particle Laser Spectroscopy," *Journal of Physical Chemistry C* 114, no. 44 (2010): 18880–18885.

32. M. P. Hughes and H. Morgan, "Dielectrophoretic Trapping of Single Sub-Micrometre-Scale Bioparticles," *Journal of Physics D: Applied Physics* 31, no. 17 (1998): 2205.

33. N. G. Green and H. Morgan, "Dielectrophoresis of Submicrometer Latex Spheres. 1. Experimental Results," *Journal of Physical Chemistry B* 103, no. 1 (1999): 41–50.

34. I. Ermolina and H. Morgan, "The Electrokinetic Properties of Latex Particles: Comparison of Electrophoresis and Dielectrophoresis," *Journal of Colloid and Interface Science* 285, no. 1 (2005): 419–428.

35. D. J. Bakewell and H. Morgan, "Dielectrophoresis of DNA: Time- and Frequency-Dependent Collections on Microelectrodes," *IEEE Transactions on NanoBioscience* 5, no. 1 (2006): 1–8.

36. N. G. Green, A. Ramos, and H. Morgan, "AC Electrokinetics: A Survey of Sub-Micrometre Particle Dynamics," *Journal of Physics D: Applied Physics* 33, no. 6 (Mar. 2000): 632, https://doi.org/10.1088/0022-3727/33/6/308.

37. H. Morgan and N. Green, *AC Electrokinetics: Colloids and Nanoparticles*, ser. Microtechnologies and Microsystems Series (Research Studies Press, 2003), https://books.google.es/books?id=FKhPkgEACAAJ.

38. D. J. Bakewell and H. Morgan, "Quantifying Dielectrophoretic Collections of Sub-Micron Particles on Microelectrodes," *Measurement Science and Technology* 15, no. 1 (2003): 254.

39. Y.-H. Su, M. Tsegaye, W. Varhue, K.-T. Liao, L. S. Abebe, J. A. Smith, R. L. Guerrant, and N. S. Swami, "Quantitative Dielectrophoretic Tracking for Characterization and Separation of Persistent Subpopulations of Cryptosporidium Parvum," *Analyst* 139, no. 1 (2014): 66–73.

40. C. V. Crowther, S. H. Hilton, L. Kemp, and M. A. Hayes, "Isolation and Identification of Listeria Monocytogenes Utilizing DC Insulator-Based Dielectrophoresis," *Analytica Chimica Acta* 1068 (2019): 41–51.

41. K. B. Taas, B. Oh, M. Son, et al., "Revolutionizing Dielectrophoresis: Unveiling the Potential of 3D Electrodes," *BioChip Journal* 20, no. 2 (Apr. 2026): 203–235, https://doi.org/10.1007/s13206-025-00242-x.

42. S. Stanke, F. F. Bier, and R. Hölzel, "Fluid Streaming Above Interdigitated Electrodes in Dielectrophoresis Experiments," *Electrophoresis* 32, no. 18 (2011): 2448–2455.

43. J. C. Crocker and D. G. Grier, "Methods of Digital Video Microscopy for Colloidal Studies," *Journal of Colloid and Interface Science* 179, no. 1 (1996): 298–310.

44. S. L. Dettmer, U. F. Keyser, and S. Pagliara, "Local Characterization of Hindered Brownian Motion by Using Digital Video Microscopy and 3D Particle Tracking," *Review of Scientific Instruments* 85, no. 2 (2014): 023708.

45. M. Badieirostami, M. D. Lew, M. A. Thompson, and W. E. Moerner, "Three-Dimensional Localization Precision of the Double-Helix Point Spread Function Versus Astigmatism and Biplane," *Applied Physics Letters* 97, no. 16 (2010): 161103.

46. Y. Shechtman, L. E. Weiss, A. S. Backer, S. J. Sahl, and W. E. Moerner, "Precise Three-Dimensional Scan-Free Multiple-Particle Tracking over Large Axial Ranges with Tetrapod Point Spread Functions," *Nano Letters* 15, no. 6 (2015): 4194–4199.

47. F. Alnaimat, S. Ramesh, A. Alazzam, A. Hilal-Alnaqbi, W. Waheed, and B. Mathew, "Dielectrophoresis-Based 3D-Focusing of Microscale Entities in Microfluidic Devices," *Cytometry Part A* 93, no. 8 (2018): 811–821.

48. L. Challier, J. Lemarchand, C. Deanno, et al., "Printed Dielectrophoretic Electrode-Based Continuous-Flow Microfluidic Systems for Particles 3D-Trapping," *Particle & Particle Systems Characterization* 38, no. 2 (2021): 2000235.

49. M. Haapalainen, V. Kaikkonen, and A. Mäkynen, "In-Depth Imaging of Dielectrophoresis by Digital In-Line Holographic Microscopy," *Procedia Engineering* 5 (2010): 1336–1339.

50. S. Geissbuehler, A. Sharipov, A. Godinat, et al., "Live-Cell Multiplane Three-Dimensional Super-Resolution Optical Fluctuation Imaging," *Nature Communications* 5 (2014): 5830.

51. B. Louis, R. Camacho, R. Bresolí-Obach, et al., "Fast-Tracking of Single Emitters in Large Volumes with Nanometer Precision," *Optics Express* 28, no. 19 (2020): 28656–28656.

52. B. Louis, C.-H. Huang, R. Camacho, et al., "Unravelling 3D Dynamics and Hydrodynamics During Incorporation of Dielectric Particles to an Optical Trapping Site," *ACS Nano* 17, no. 4 (2023): 3797–3808.

53. R. Fish, A. Carter, P. Diez-Silva, R. Delgado-Buscalioni, R. P. Pelaez, and B. Sprinkle, "Libmobility: A Python Library for Hydrodynamics at the Smoluchowski Level," *The Journal of Chemical Physics* 164, no. 4 (2026): 044121, https://doi.org/10.1063/5.0304943.

54. B. Sullivan and A. Kaszynski, "PyVista: 3D Plotting and Mesh Analysis Through a Streamlined Interface for the Visualization Toolkit (VTK)," *Journal of Open Source Software* 4, no. 37 (May 2019): 1450, https://doi.org/10.21105/joss.01450.

55. P. Ibáñez-Freire, "Uammd-Structured," https://github.com/PabloIbannez/UAMMD-structured (2025).

56. A. Castellanos, A. Ramos, A. González, N. G. Green, and H. Morgan, "Electrohydrodynamics and Dielectrophoresis in Microsystems: Scaling Laws," *Journal of Physics D: Applied Physics* 36, no. 20 (Oct. 2003): 2584, https://doi.org/10.1088/0022-3727/36/20/023.

57. S. Delong, B. E. Griffith, E. Vanden-Eijnden, and A. Donev, "Temporal Integrators for Fluctuating Hydrodynamics," *Physical Review E* 87 (Mar. 2013): 033302, https://doi.org/10.1103/PhysRevE.87.033302.

58. N. G. Green, A. Ramos, A. González, H. Morgan, and A. Castellanos, "Fluid Flow Induced by Nonuniform AC Electric Fields in Electrolytes on Microelectrodes. III. Observation of Streamlines and Numerical Simulation," *Physical Review E* 66, no. 2 (Aug. 2002): 026305, https://doi.org/10.1103/PhysRevE.66.026305.

59. P. Garcia-Sanchez, A. Ramos, N. Green, and H. Morgan, "Experiments on AC Electrokinetic Pumping of Liquids Using Arrays of Microelectrodes," *IEEE Transactions on Dielectrics and Electrical Insulation* 13, no. 3 (June 2006): 670–677, https://ieeexplore.ieee.org/document/1657983/.

60. J. W. Swan and J. F. Brady, "Simulation of Hydrodynamically Interacting Particles Near a No-Slip Boundary," *Physics of Fluids* 19, no. 11 (Nov. 2007): 113306, https://doi.org/10.1063/1.2803837.



16136829, 2026, 58, Downloaded from https://onlinelibrary.wiley.com/doi/10.1002/smll.75129, Wiley Online Library on [10/11/2026]. See the Terms and Conditions (https://onlinelibrary.wiley.com/terms-and-conditions) on Wiley Online Library for rules of use; OA articles are governed by the applicable Creative Commons License

61. R. P. Peláez, P. Ibáñez-Freire, P. Palacios-Alonso, A. Donev, and R. Delgado-Buscalioni, "Universally Adaptable Multiscale Molecular Dynamics (UAMMD): A Native-GPU Software Ecosystem for Complex Fluids, Soft Matter, and Beyond," *Computer Physics Communications* 306 (2025): 109363, https://www.sciencedirect.com/science/article/pii/S0010465524002868.

62. C. S. Peskin, "Flow Patterns Around Heart Valves: A Numerical Method," *Journal of Computational Physics* 10, no. 2 (Oct. 1972): 252–271, https://www.sciencedirect.com/science/article/pii/0021999172900654.

63. Y. Saad and M. H. Schultz, "GMRES: A Generalized Minimal Residual Algorithm for Solving Nonsymmetric Linear Systems," *SIAM Journal on Scientific and Statistical Computing* 7, no. 3 (1986): 856–869, https://doi.org/10.1137/0907058.

64. O. Schnitzer and E. Yariv, "Macroscale Description of Electrokinetic Flows at Large Zeta Potentials: Nonlinear Surface Conduction," *Physical Review E* 86, no. 2 (Aug. 2012): 021503, https://doi.org/10.1103/PhysRevE.86.021503.

65. S. S. Seyedi and D. V. Matyushov, "Protein Dielectrophoresis in Solution," *Journal of Physical Chemistry B* 122, no. 39 (Oct. 2018): 9119–9127, https://doi.org/10.1021/acs.jpcb.8b06864.

66. W. Cao, M. Chern, A. M. Dennis, and K. A. Brown, "Measuring Nanoparticle Polarizability Using Fluorescence Microscopy," *Nano Letters* 19, no. 8 (Aug. 2019): 5762–5768, https://doi.org/10.1021/acs.nanolett.9b02402.

67. E. Yariv and T. Miloh, "Electro-Convection About Conducting Particles," *Journal of Fluid Mechanics* 595 (Jan. 2008): 163–172, https://www.cambridge.org/core/journals/journal-of-fluid-mechanics/article/abs/electroconvection-about-conducting-particles/C12BE6369B2BE8887594E1DBB9E651A2.

68. T. Miloh, "Dipolophoresis of Nanoparticles," *Physics of Fluids* 20, no. 6 (June 2008): 063303, https://doi.org/10.1063/1.2931080.

69. B.-Y. Shih, S. Fransen, E. Valvo, et al., "Not Only Dielectrophoresis: The Crucial Role of Electrokinetic Phenomena in a Dielectric Particle's Response to an Oscillating Electric Field," *Journal of Electrostatics* 133 (Jan. 2025): 104009, https://www.sciencedirect.com/science/article/pii/S0304388624001165.

70. R. Fernández-Mateo, P. García-Sánchez, V. Calero, H. Morgan, and A. Ramos, "Stationary Electro-Osmotic Flow Driven by AC Fields Around Charged Dielectric Spheres," *Journal of Fluid Mechanics* 924 (Oct. 2021): R2, https://www.cambridge.org/core/journals/journal-of-fluid-mechanics/article/stationary-electroosmotic-flow-driven-by-ac-fields-around-charged-dielectric-spheres/4D37A1F8B31B7712D0855E0F9E6DCF54.

71. H. Zhao and H. H. Bau, "The Polarization of a Nanoparticle Surrounded by a Thick Electric Double Layer," *Journal of Colloid and Interface Science* 333, no. 2 (May 2009): 663–671, https://www.sciencedirect.com/science/article/pii/S0021979709001374.

72. A. Abdelghany, Y. Ichikawa, and M. Motosuke, "Tuning AC Electrokinetic Flow to Enhance Nanoparticle Accumulation in Low-Conductivity Solutions," *Advanced Materials Interfaces* 10, no. 34 (2023): 2300478, https://onlinelibrary.wiley.com/doi/abs/10.1002/admi.202300478.

73. X. Chen, X. Chen, Y. Peng, L. Zhu, and W. Wang, "Dielectrophoretic Colloidal Levitation by Electrode Polarization in Oscillating Electric Fields," *Langmuir* 39, no. 19 (May 2023): 6932–6945, https://doi.org/10.1021/acs.langmuir.3c00759.

74. K. Trofymchuk, A. Reisch, P. Didier, et al., "Giant Light-Harvesting Nanoantenna for Single-Molecule Detection in Ambient Light," *Nature Photonics* 11 (2017): 657–663.

## Supporting Information

Additional supporting information can be found online in the Supporting Information section.

**Supporting File**: smll75129-sup-0001-SuppMat.pdf.



16136829, 2026, 58, Downloaded from https://onlinelibrary.wiley.com/doi/10.1002/smll.75129, Wiley Online Library on [10/11/2026]. See the Terms and Conditions (https://onlinelibrary.wiley.com/terms-and-conditions) on Wiley Online Library for rules of use; OA articles are governed by the applicable Creative Commons License